DETERMINATION OF SPECTRAL SIGNATURES OF SUBSTANCES IN NATURAL WATERS

V. Klemas, W. Philpot and G. Davis
College of Marine Studies
University of Delaware
Newark, Delaware 19711

March 1, 1978
Final Report
NASA GRANT NSG 1149

Prepared for
NATIONAL AERONAUTICS AND SPACE ADMINISTRATION
LANGLEY RESEARCH CENTER
HAMPTON, VIRGINIA 23665

I. Introduction

Concern for the oceanic environment has increased considerably over the past several years and has led to a general agreement on the need to control pollution in the ocean and near-shore waters. However, effective control requires an effective means of monitoring pollution. This task is extraordinarily difficult by conventional oceanographic methods for several reasons:

1) The cost of obtaining the necessary data would be enormous.

2) Even if sufficient funds were available, ships are too slow and standard oceanographic methods too involved for adequate coverage of large areas. Frequent, repetitive coverage presents even more of a problem in terms of ship operations.

3) Effective monitoring requires a fast response time on the part of the monitoring agency. Except for limited applications this is contrary to the nature of ship-based work.

In spite of these limitations, ship-based work remains the most effective way of collecting the data necessary for the purpose of monitoring deep ocean areas. For phenomena in the surface layer*, however, optical remote sensing offers a promising alternative. It offers the possibility of fast, large scale coverage at a relatively low cost, in short, exactly the requirements of an effective monitoring system.

It is the object of this study to explore the possibility of using the spectral characteristics of the upwelling light from water for the

*The surface layer refers to that layer of water which is responsible for the major portion of light returned to the atmosphere. This layer may range in depth from 25m in clear ocean water to less than one meter in an estuary.

purpose of ocean water quality monitoring. The work was broken into several broad tasks which are as follows:

1) Definition of a remotely measured spectral signature of water. -- This was the topic of the progress report submitted on June 3, 1977. That work will be summarized here.

2) Collection of field data and testing of the signature analysis. -- The only data used to test the effectiveness of the model was also reported in the June 3, 1976 progress report. Attempts were made to collect additional data at the duPont iron-acid waste dumpsite and at the Philadelphia sewage sludge dumpsite. Although all three missions were largely successful both in terms of remote sensing data and ground truth data, the ship-board measurements of upwelling and downwelling spectra were too noisy (because of clouds and ship motion) to be useful in verifying the spectral signature technique. The data for the duPont site was reported in the October 18, 1976 progress report while the data for the sewage sludge site was included in the June 3, 1977 report. The analysis of the remaining field data was performed by NASA Langley personnel and has been reported elsewhere (Lewis and Collins, 1977; Johnson et al., 1977).

3) Investigate the possibility of using Landsat data for the identification of substances in water. -- The attempt to extract spectral signatures of acid waste and sediment was successful. This task will be covered in detail in this report.

II. Spectral Signature of Water for Remote Sensing

The utility of spectral remote sensing for water quality monitoring depends on the validity of the premise that water color is related to water quality. Many of the changes in apparent water color are, in fact, due to changes in the scattering and absorption properties of the water which are themselves manifestations of differences in the water content, i.e. variations in the concentration and distribution of suspended sediments, plankton, pollutants and the like. Unfortunately, the apparent water color is also a function of the illumination conditions and the reflectivity of the water surface. The former is related to the sun angle, solar radiance and the skylight radiance distribution, while the latter is largely dependent upon sea state and the presence or absence of surface slicks. This points to the need for a measure of water color which is sensitive to changes in the optical properties of the water but insensitive to changes in the incident light field.

The possible approaches to this problem range from the purely empirical (Arvesen 1973, Maul et al. 1974, Mueller 1976) to the purely theoretical (Kattawar and

Plass 1972, 1973, McCluney 1974, Gordon et al. 1975). Each approach is beset with its own set of problems. The theoretical models do not lend themselves easily to the problem of remote sensing. The optical processes in natural waters, particularly the scattering process, are such that it is possible to develop a predictive model for the upwelling radiation from the water given the incident radiance distribution and the optical characteristics of the water. However, the inverse problem of determining the optical characteristics given the incident and upwelling radiance distribution is troublesome at best. The inverse problem has only been solved analytically for an axially symmetric light field (Zaneveld and Pak 1972, Zaneveld 1974) which is not really appropriate for the upper layers of the water and is therefore unsuited to the needs of remote sensing. Jain and Miller (1976) have taken an interesting approach to the problem. Using Hulbert's (1943) two-flow model, they adjust the pertinent optical parameters of the water until the calculated upwelling radiation agrees with the measured values. The adjusted optical constants agree quite well with measured values in their work. This may well prove to be a fruitfull approach although, for anything more complex than the two-flow model it would be rather cumbersome.

Empirical methods avoid the complexities of analytical models but occassionally lead to ambiguous results. This ambiguity generally arises because the real optical properties of the water are treated indirectly. Thus, when Tabor (1974) attempted to use a ratio technique for measuring chlorophyll concentration which had been suggested by Arvesen et al. (1973), he found that he obtained erroneous results whenever fairly high concentrations of terriginous sediments were present. Maul and Gordon (1975) had similar problems with a ratio technique for LANDSAT data. Still, the empirical approach lends itself readily to remote sensing applications where there is rarely any a priori knowledge of the optical properties of the water.

The approach which will be taken here is semi-empirical. A radiative transfer model will be used to trace the upwelling and downwelling radiation across the air-water interface, but the interactive processes of the light with the water will be treated empirically.

2.1 Volume Reflectance

The volume reflectance ρ_v will be defined here as the ratio of upwelling radiance in the direction θ', ϕ' to

the downwelling irradiance just below the water surface:

$$\rho_v = \frac{N_u'(\theta,\phi')}{H_d'} \qquad (2.1)$$

The assumption here is that, since the volume reflectance is directly related to the inherent optical properties of the water, it is itself an inherent property of the water. Insofar as the absorption and scattering properties of the water are measures of the water quality, the volume reflectance should also be indicative of water quality. Finally, the accuracy of the measurement of the remotely sensed volume reflectance depends primarily on the accuracy of the measurement of the incident and upwelling radiation (and, of course, on the accuracy of the model). Using upwelling radiance rather than irradiance (or, more properly, emittance) is a concession to the realities of remote sensing. A remote sensing instrument is restricted to measurements of upwelling radiance because of its limited acceptance angle and because of the necessity of avoiding specularly reflected sunlight.

For remote sensing applications ρ_v must be related to measurements which can be made above the water surface. In the following discussion the primed symbols refer to

quantities in water, the unprimed symbols to quantities in air. The subscripts u and d refer to upwelling and downwelling respectively. The upwelling radiance just above the water surface $N_u(\theta,\phi)$ is equal to the transmitted portion of the upwelling radiance below the water surface $(1-\rho'(\theta'))N'_u(\theta',\phi')$ plus the downwelling sky radiance reflected by the water surface $\rho(\theta)N_d(\theta,\phi)$ (figure 2.1B)

$$N_u(\theta,\phi) = \frac{1}{\eta^2}(1-\rho'(\theta'))N'_u(\theta',\phi') + \rho(\theta)N_d(\theta,\phi) \qquad (2.2)$$

where $\eta = n'/n$

The factor $1/\eta^2$ is present to account for the change in ray geometry across the interface (Nicodemus 1963). In essence, the radiance emerging from the water will be decreased by the factor $1/\eta^2$ due to refraction alone.

The downwelling radiance in water, $N'_d(\theta',\phi')$, is equal to the transmitted downwelling sky radiance, $(1-\rho(\theta))N_d(\theta,\phi)$, plus the internally reflected upwelling radiance, $\rho'(\theta')N'_u(\theta',\phi')$, (Figure 2.1A),

$$N'_d(\theta',\phi') = \eta^2(1-\rho(\theta))N_d(\theta,\phi) + \rho'(\theta')N'_u(\theta',\phi') \qquad (2.3)$$

n = index of refraction in air

n'= index of refraction in water

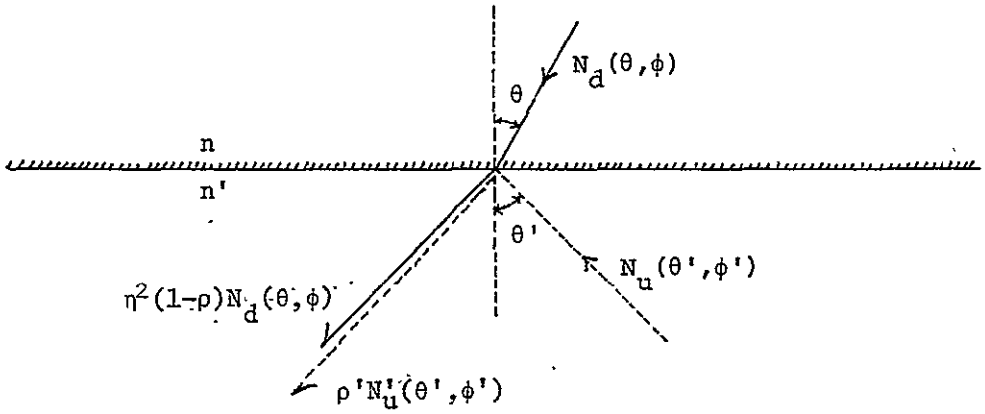

Figure 2.1A - Downwelling radiance

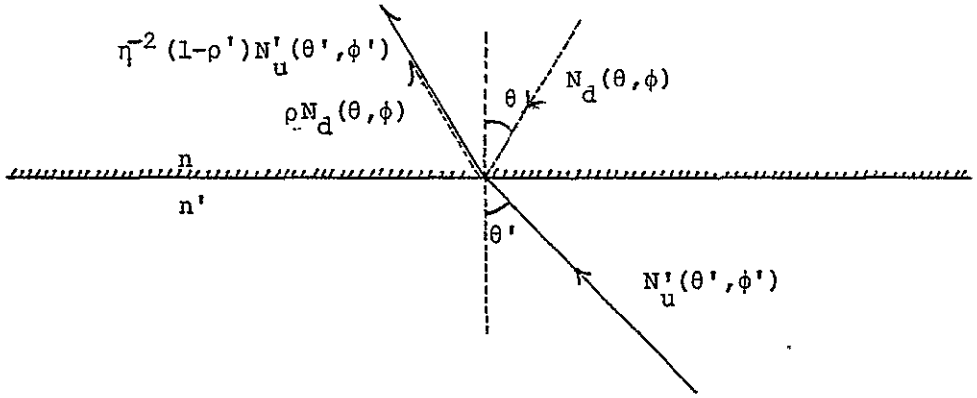

Figure 2.1B - Upwelling Radiance

The total downwelling irradiance on a horizontal plane in water is given by integrating equation 2.3 over the entire upward hemisphere,

$$H_d' = \int_0^{2\pi}\int_0^{\pi/2} N_d'(\theta',\phi')\cos\theta'\sin\theta'd\theta'd\phi$$

$$= \eta^2\int_0^{2\pi}\int_0^{\theta_c'}(1-\rho(\theta))N_s(\theta,\phi)\cos\theta'\sin\theta'd\theta'd\phi'$$

$$+ \eta^2(1-\rho(\theta_\odot))N_\odot(\theta_\odot,\phi_\odot)\cos\theta_\odot'\Omega_\odot' \qquad (2.4)$$

$$+ \int_0^{2\pi}\int_0^{\pi/2}\rho'(\theta')N_u'(\theta',\phi')\cos\theta'\sin\theta'd\theta'd\phi'$$

where the downwelling radiance, N_d, has been separated into solar, $N_\odot$, and sky, N_s, radiance. The solid angle subtended by the sun is $\Omega_\odot$. The terms for skylight and sunlight may be converted to unprimed (air) coordinates by using the relationship

$$\cos\theta\sin\theta d\theta = \eta^2\cos\theta'\sin\theta'd\theta' \qquad (2.5)$$

which is derived directly from Snell's law. Also, if we make the usual assumption that both the sky and ocean may be approximated by Lambertian sources, then N_s and N_u' are both constant and may be removed from the integrals.

$$H'_d = 2\pi N_s(\theta_{ob}) \int_0^{\pi/2} (1-\rho(\theta))\cos\theta\sin\theta d\theta$$
$$+ (1-\rho(\theta_\odot))N_\odot \cos\theta_\odot \Omega_\odot \qquad (2.6)$$
$$+ 2\pi N'_u(\theta'_{ob})) \int_0^{\pi/2} \rho'(\theta')\cos\theta'\sin\theta' d\theta'$$

where θ_{ob} is the angle of observation for the remote sensing instrument.

For a perfectly calm sea the reflectance coefficients, $\rho'(\theta')$ and $\rho(\theta)$, are given directly by Fresnel's equations. For other sea states, Gordon (1969) has generated time-averaged reflectances for windspeeds up to 38 knots. Austin (1974) presents these in tabular form. Using these coefficients it is possible to perform the integrations in equation 2.6 for any reasonable sea-state. Since, as the sea state increases it becomes increasingly difficult to avoid excessive problems with foam, whitecaps and specularly reflected sunlight, it would be best if measurements could be restricted as far as possible to calm sea conditions.

Using Fresnel's equations (assuming unpolarized light) to evaluate the integrals and substituting for $N'_u(\theta',\phi')$ using equation 2.1, we have

$$H'_d = 2\pi N_s(\theta_{ob})(.466) + (1-\rho(\theta_\odot))N_\odot \cos\theta_\odot \Omega_\odot + 2\pi\eta^2\left(\frac{N_u(\theta_{ob}) - \rho(\theta_{ob})N_s(\theta_{ob})}{(1-\rho'(\theta'_{ob}))}\right)(.240) \quad (2.7)$$

Finally, Combining equations 2.2 and 2.7 we arrive at an expression for the volume reflectance which is entirely in terms of quantities measured above the water surface:

$$\rho_v = \frac{\eta^2(N_u(\theta_{ob}) - \rho(\theta_{ob})N_s(\theta_{ob}))}{(1-\rho'(\theta'_{ob}))\left[2\pi N_s(.466)+(1-p(\theta_\odot))\cos\theta_\odot\, N_\odot\Omega_\odot + 2\pi N'_u(\theta'_{ob})(.240)\right]} \quad (2.8)$$

where $N'_u(\theta'_{ob}) = \left(\frac{N_u(\theta_{ob}) - \rho(\theta_{ob})N_s(\theta_{ob})}{(1-\rho'(\theta'_{ob}))}\right)\eta^2$

2.2 Verification of volume reflectance as a signature

2.2.1 Experiments

The volume reflectance, ρ_v, is intended for use as a signature of a water mass and as such should be sensitive to changes in the optical properties of the water yet insensitive to changes in the incident light field. As a preliminary test of the validity of ρ_v as a signature, two

simultaneous experiments were conducted at Roosevelt Inlet, Delaware on August 31, 1976. The first was designed to test the stability of ρ_v for a stable water mass under a changing light field. The second experiment was designed to test the sensitivity of ρ_v to changes in the water itself. For the first, tne target was the water in a tank. For the second, the target was the water by the floating dock at the University of Delaware's Lewes facility just inside Roosevelt Inlet. The optical properties of the water at this point vary quite significantly over a tidal cycle. This dockside water was also used for the tank experiment..

The tank in the first experiment was one meter square by half a meter deep. The inside of the tank was painted flat black to reduce reflections from the bottom and sides of the tank. To be certain that the tank itself did not affect the radiance measurements, the dimensions of the tank had to be much greater than an attenuation length of the water. An attenuation length is defined as the water path required to reduce a beam of light by a factor of 1/e (Duntley 1974). The beam transmittance of the water in the tank was 26% for a 10cm path and, from the Lambert-Beer law,

$$\frac{I}{I_o} = .26 = e^{-cz} = e^{-0.1c} \qquad (2.9)$$

from which we have the attenuation coefficient, $c \approx 13.4 m^{-1}$. For one attenuation length, z_a, we have

$$\frac{I}{I_o} = e^{-1} = e^{-13.4 z_a} \qquad (2.10)$$

$$\Longrightarrow z_a = 7.5 cm$$

which is sufficiently less than the smallest dimension of the tank (50cm). The depth of the dock-side water varied with the tide but was always deep enough that bottom effects could be ignored.

The day was very nearly ideal. It was extremely clear all day with only an occasional light breeze. The water in the tank was always glassy smooth during the measurements and the dockside water had, at the very worst, a lightly rippled surface. For this day, at least, Fresnel's equations should be valid as an estimate of surface reflection.

2.2.2 Radiance Measurements

The radiance measurements were made with a United Detector Technology scanning spectroradiometer. This instrument is described in detail in Appendix A. The instrument could not be used to measure global irradiance

directly due to its very directional angular response. The radiometer was used only with a Gershun tube in place. A Gershun tube is a device which directly limits the solid angle viewed by the radiometer (Gershun 1939). In this case the field of view was restricted to .0153 steradians.

Solar Irradiance - $H_\odot$ - To measure the solar irradiance the radiometer is aimed directly at the sun. Since the solid angle subtended by the sun is considerably less than the solid angle viewed by the instrument, the measurement is essentially that of the solar irradiance on a plane perpendicular to the sun's rays. The measurement is fractionally higher than it should be since the radiometer views the skylight near the sun, but the error is relatively small. In equation 2.7, $N_\odot \Omega_\odot = H_\odot$.

Zenith Sky Radiance - N_z - The viewing angle for the measurement of the upwelling radiance determines the viewing angle for the sky radiance, that is, the skylight measurement should be made on that portion of the sky which is the source of the reflected portion of the upwelling signal. Since, in this case the target radiance was always the nadir radiance, the sky radiance was always measured at zenith. In equation 2.7, $N_s = N_z$.

Upwelling Radiance from the Water - $N_u(\theta_{ob})$ - The radiometer viewed the nadir, i.e., $\theta_{ob}=0$. The basic precept in choosing the angle of observation for upwelling light is to avoid sun glitter. Beyond this it is a matter of minimizing the proportion of surface reflection in the total upwelling. Figure 2.2 shows reflectance coefficient curves for reflectance at the air-water interface (Austin 1974). The reflectance coefficient in air does not increase substantially until the angle of observation reaches about 50° for any sea state. Similarly, for moderate sea states (wind speeds of 4m/s ≅ 8knots) reflection losses at the surface do not increase until about 30° in water which corresponds to an observation angle of about 40° in air. Based on these values any viewing angle up to 40° should suffice as long as the sun glitter is avoided. There are, however, other considerations. At Brewster's angle -- 53.3° in this case -- only light polarized perpendicular to the plane of incidence is reflected. Thus, viewing at or near Brewster's angle on a calm day with a polarizing filter oriented to remove the perpendicularly polarized light would effectively remove the specularly reflected skylight. Unfortunately, since nearly half of the upwelling signal from below the water surface would also be removed by the filter this approach was impractical for the present work.

The resulting signal would have been too low for the sensitivity of the radiometer.

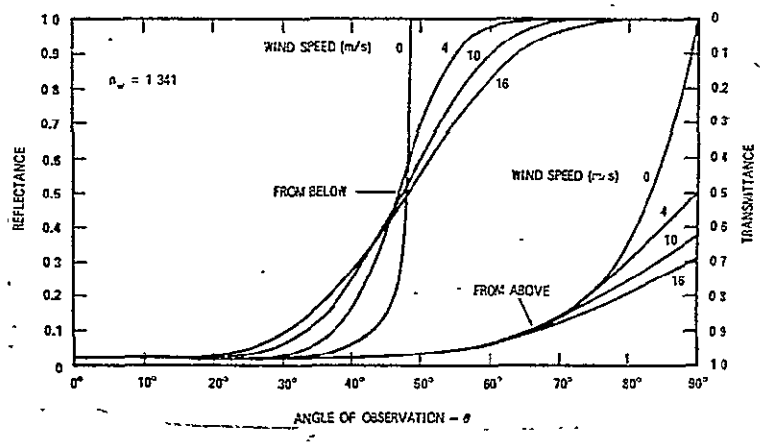

Figure 2.2 - Reflectance and transmittance of water-air boundary as a function of the angle of observation for several windspeeds (Austin 1974).

A second consideration is that sky radiance on a clear day is at a minimum in the solar plane at 90° or less from the sun. Figure 2.3 shows a typical radiance distribution for a clear day (Boileau 1964). (Figure 2.3 also indicates the inadequacy of the assumption that the sky is a Lambertian source on a clear day.) The minimum is fairly broad so the precise angle of observation is not critical. Measuring at this angle has the advantage of reducing the skylight component without drastically reducing the total signal. This method was not attempted in the present work because at the time of the experiment I did not realize that this minimum existed.

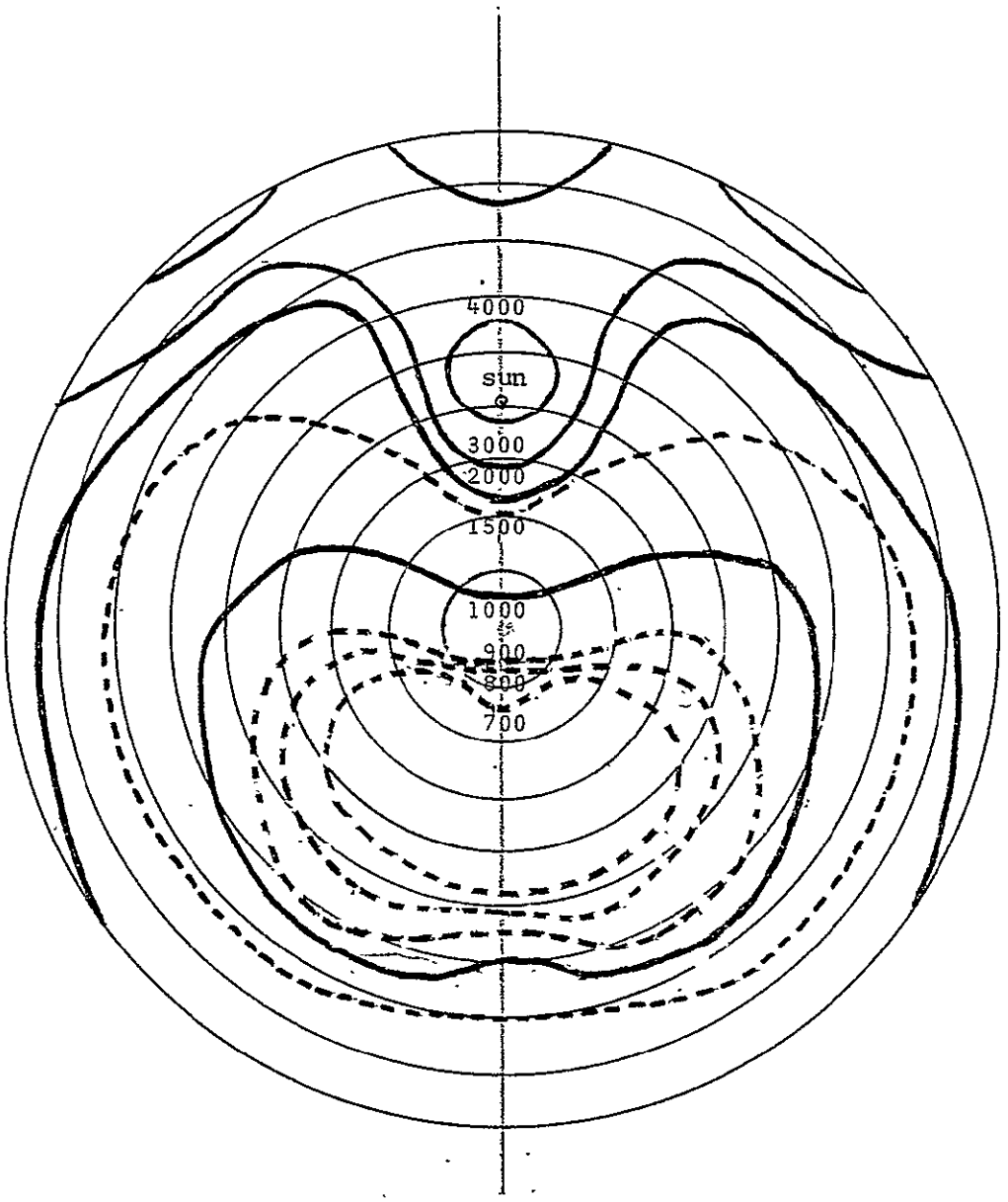

Figure 2.3 - Skylight radiance distribution on a clear day. The origin represents the local zenith. The vertical line marks the solar plane. The solar zenith angle is 40.5°. The values are in ft.-lumens. (Boileau 1964)

A final point is that there may be some advantage to an angle of observation which is constant relative to the sun angle. If, for instance, contrary to the assumption being made here, the volume reflectance exhibits an angular dependence due to the scattering process in the water then, on a clear day, the ideal might be to adjust the angle of observation in order to maintain a constant (single) scattering angle.

2.2.3 Procedure

A series of radiance measurements was made at hourly intervals from 1100 to 1700 hours on August 31,1976. During this time the solar zenith angle ranged from 30.5° to 67.5°. The procedure for each series was as follows:

1. Measure the zenith sky radiance.
2. Measure the solar irradiance.
3. Stir the tank water to resuspend the larger particles and disrupt any stratification that may have set up since the last stirring.
4. Measure the transmissivity of the tank water.
5. Measure the upwelling radiance from the tank.
6. Measure the transmissivity of the dockside water.
7. Measure the upwelling radiance of the dockside

water.

8. Measure the solar irradiance.

9. Measure the zenith sky radiance.

With practice, each series could be completed in about 35 minutes.

The radiance and irradiance spectra are presented in tabular form in Appendix B. Each spectrum is an average of at least four and usually five scans. The variability among the spectra for each measurement was usually less than ±2% for the visible wavelengths. This includes the uncertainty in reading the values from strip-chart recordings.

2.2.4 Results

The volume reflectance may now be evaluated. Since the observation angle for this experiment was always zero ($\theta_{ob}=0$), both $\rho(\theta)$ and $\rho'(\theta')$ are approximately equal to .02 from Fresnel's equations. In measuring the radiance from the water in the tank, however, the radiometer was only about 2 feet above the water surface. Since the field of view was .0153 steradians and the area of the insruments body was ~220cm^2, it was thus shading the water from about one half of the zenith skylight that would have been reflected into the sensor from the water surface. This

reduces the effective reflection coefficient in the numerator and in the last term in the denominator of equation 2.8 to .01. Finally, equation 2.8 may be reduced to:

$$\rho_v = \frac{\eta^2 (N_u - .01N_z)}{.98\left[2\pi(.466)N_z + (1-\rho(\theta_\odot))\cos\theta_\odot N_\odot \Omega_\odot\right] + 2\pi\eta^2\left[N_u - .01N_z\right](.240)} \quad (2.11)$$

Setting $\eta = 1.341$ and consolidating constants gives:

$$\rho_v = \frac{1.798\ (N_u - .01N_z)}{2.87N_z + .98(1-\rho(\theta_\odot))\cos\theta_\odot N_\odot \Omega_\odot + 2.71(N_u - .01N_z)} \quad (2.12)$$

for the tank data and

$$\rho_v = \frac{1.798\ (N_u - .02N_z)}{2.87N_z + .98(1-\rho(\theta_\odot))\cos\theta_\odot N_\odot \Omega_\odot + 2.71(N_u - .02N_z)} \quad (2.13)$$

for the dockside data.

2.2.5 Tank data

Figures 2.4 and 2.5 show the tank upwelling radiances and volume reflectances respectively. The breaks in the curves at 700nm represent the point at which the radiometer changes filters between the visible and infrared

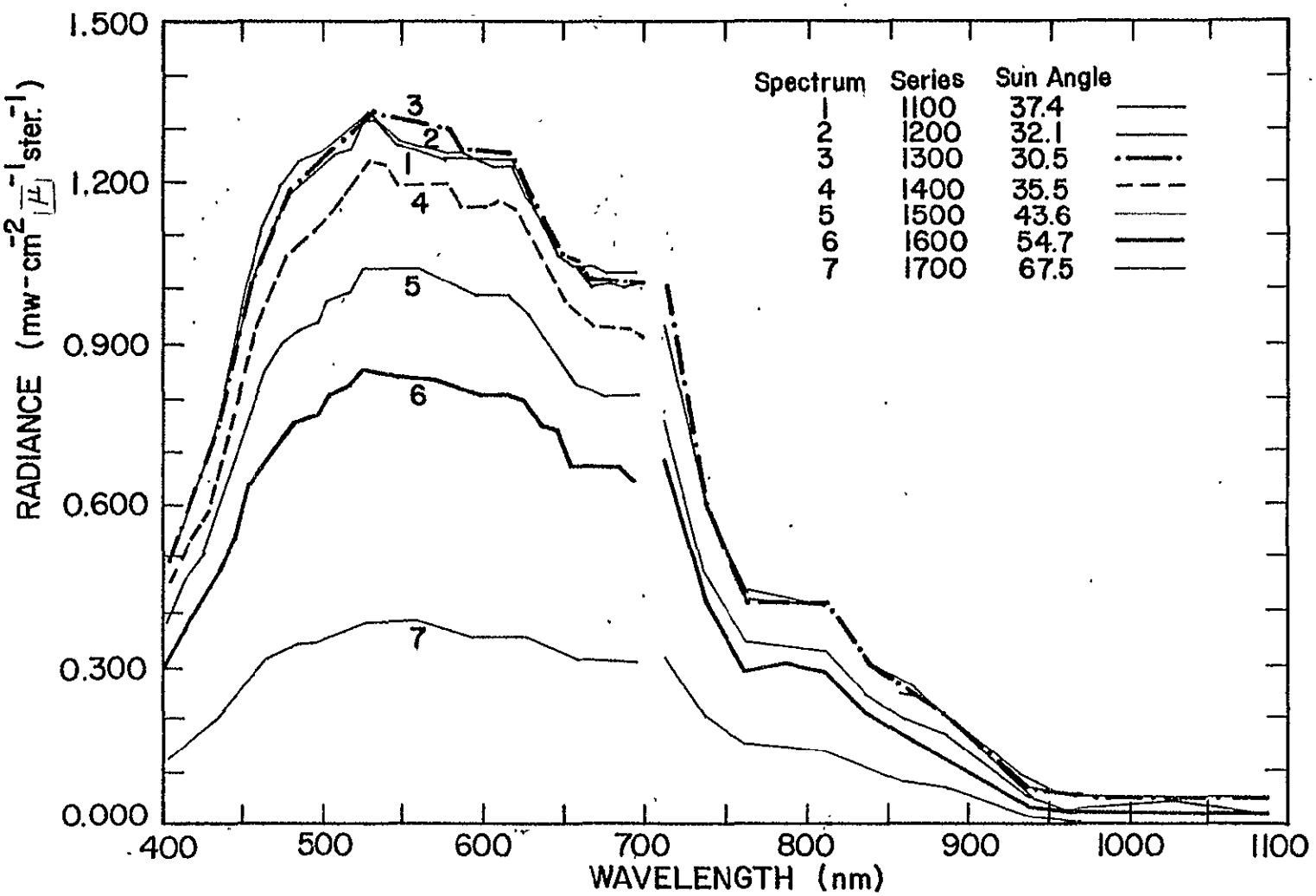

Figure 2.4 - Upwelling radiance from the tank water.

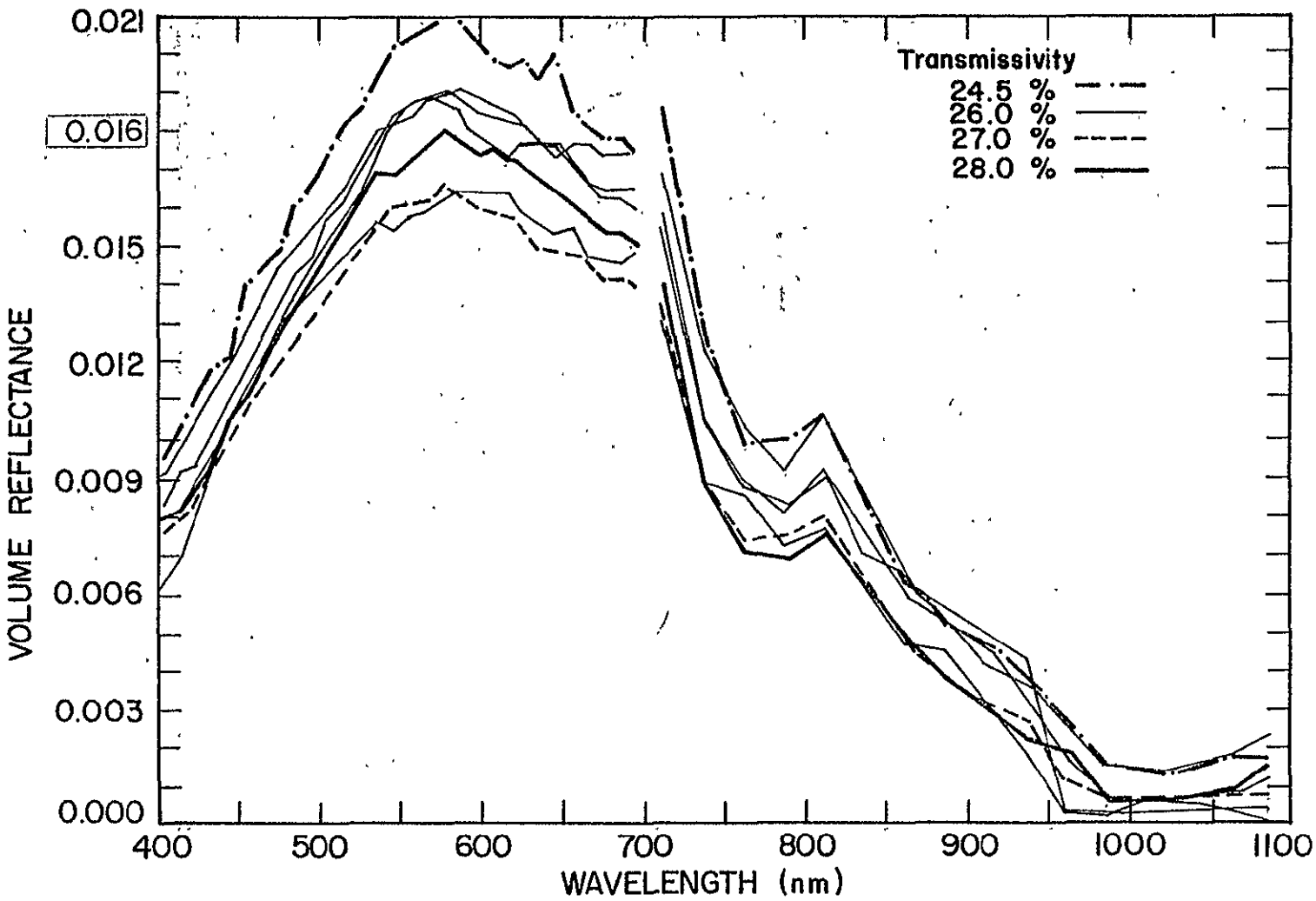

Figure 2.5 - Volume reflectance from tank water.

portions of the spectrum.

The shapes of the curves of upwelling, N_u, are very similar but vary tremendously in total intensity. There is an obvious relationship to sun angle -- the top four curves are for the mid-day readings when the sun was at or near the apex while the bottom three curves correspond, in descending order, to increasing solar zenith angles. The percent variation in the data (defined here as the ratio of one standard deviation to the mean) is about ±33% in the visible.

In contrast, the volume reflectance curves in figure 2.5 form a much tighter group, exhibiting about ±9% variation through most of the visible region. Furthermore, there is no apparent dependence on sun angle. Instrumental error can account for no more than ±5% of the variability in the volume reflectance. A large part of the variability must come from either the experimental design, an inadequacy in equation 2.9 as a definition of the volume reflectance or changes in the water itself. The most likely source of error arising from experimental design is in the possible effects of the tank on the signal. This possibility was examined in section 2.2.1 and found to be unlikely. Measurements of the upwelling radiance, N_u, were always made

at the center of the tank. The nearest boundary of the tank was greater than 7 attenuation lengths from the point of measurement. Shading of the water by the sides of the tank is negligible except at very high solar zenith angles. Even at 70° the effect should not be very significant. The tank itself was, inevitably, shaded from some of the skylight by the instrument -- probably no more than 10% at the very worst. This is negligible. Care was taken to insure that no part of the tank was shaded from direct sunlight.

The second possible source of error is an inadequacy in equation 2.9 as a definition of the volume reflectance. The assumptions which are most questionable are the assumption of a Lambertian sky and the assumption that the volume reflectance is an invariant property of the water. As was noted above, sky radiance is not typically Lambertian. Figure 2.3 shows the sky radiance distribution for a cloudless but hazy day based on measurements made by Boileau (1964). The sky is brightest near the sun (θ=40.5°). Sky brightness decreases away from the sun and increases toward the horizon. There is a broad minimum in the solar plane and, in this case, about 70° from the sun. (Kagan and Kondrat'ev (1971) have published tables of sky radiance distribution for a large range of sun angles on clear

days.) Not only is the sky not Lambertian but there is a certain amount of spectral variability over the whole sky (Taylor and Kerr 1941). Yet Stamm and Langel (1961) observed "no significant change in the visible spectrum of upwelling radiation because of sky conditions." They concluded that only changes in the total irradiance were of significance.

To test the possibility that the assumption of a Lambertian sky caused a serious over- or underestimate of the total skylight irradiance, the coeffient of the skylight component in the denominator of equation 2.12 was arbitrarily varied from 0 to three times the predicted value. At no point did the variability in the data decrease significantly. Farther from the predicted value the variability increased significantly. It would appear then that, at least for this day, the approximation of a Lambertian sky was valid.

This leaves us with the second possible source of error: the assumption that the volume reflectance is an invariant property of the water. The most likely mechanism for non-invariance of the volume reflectance would be the strong anisotropy of scattering in the water which may induce an angular dependence in the volume scattering. There is no clear suggestion of this in the data -- there is

no clear angular dependence. Still, this possibility exists and will be explored in considerable detail in section III.

Actually, the variability in the volume reflectance curves seems to have come from changes in the water itself. The only measure of this change is the transmissivity which was measured immediately after stirring and immediately before measurement of the upwelling radiance. At the time of the experiment I assumed that the variation in the transmissivity of 3.5% would be negligible. (The meter of the transmissometer can only be read accurately to 0.5%.) Yet, as is shown in figure 2.5, the curves seem to group according to the transmissivity values with the exception of the one low curve for 26% transmissivity water. Ignoring this one curve for a moment,* the remaining curves are strikingly well grouped. In particular, the three remaining curves for 26% transmissivity water are very similar. The similarity is all the more striking when one takes into account the fact that these represent measurements made

---

*This curve may be low due to experimental error. The gain control on the radiometer was inadvertantly set on an uncalibrated scale during the measurement of N_u. The data was later corrected by comparing the uncalibrated setting to a calibrated scale. Although to the best of my knowledge the corrected values are accurate, some error may have cropped up in the process of recalibration.

throughout the day and from almost the entire range of sun angles. The curves are for the 1100, 1500 and 1700 series with sun angles of 37.4°, 43.6° and 67.5° respectively.

Apparently, in spite of vigorous stirring prior to each measurement, the suspension of particles in the water was not quite constant through the day. Some process other than settling (flocculation, biological activity) may have affected the optical properties of the water. It appears likely that the volume reflectance is responding to these relatively small changes in the water itself. Unfortunately, without far more extensive measurements of the optical properties of the water in the tank or at least a much larger data set, it is impossible to do more than note the trend. Still, it is worth observing that if the three curves for 26% transmissivity water are indicative of the ultimate accuracy of the volume reflectance measurement, the variability in the measurement is considerably less than ±5%, i.e. well within experimental error.

2.2.6 Dockside data

The second experiment was designed to show the sensitivity of the volume reflectance to changes in the water. A significant change should exceed the uncertainty

in the measurement itself. From the results of the tank experiment the uncertainty in the measurement cannot be set less than ±9%. This is probably a conservative estimate but, given the rather limited data set, a conservative estimate is necessary.

Figures 2.6 and 2.7 show the spectral upwelling radiance and volume reflectance respectively of the dockside water. As with the tank data the percent variation in the upwelling spectra (figure 2.6) is around ±33% in the visible. As before, there is also a marked relationship to the solar zenith angle apparent in the data. With the dockside water, however, the curves fall into two distinct groups based on the shape of the spectra. The spectra from the morning (curves 1 and 2 in figure 2.6) are broadly peaked with a maximum at ≈590nm. The afternoon spectra (curves 3-7) are more narrowly peaked with maxima at ≈575nm. The difference in shape alone is probably basis enough to determine that two different water types were being observed. Although the total intensity of the incident light changed a great deal throughout the day, the spectral distribution of the light did not change very much and certainly not over the period of one hour at midday. Hence, one would not expect a noticeable change in the shape

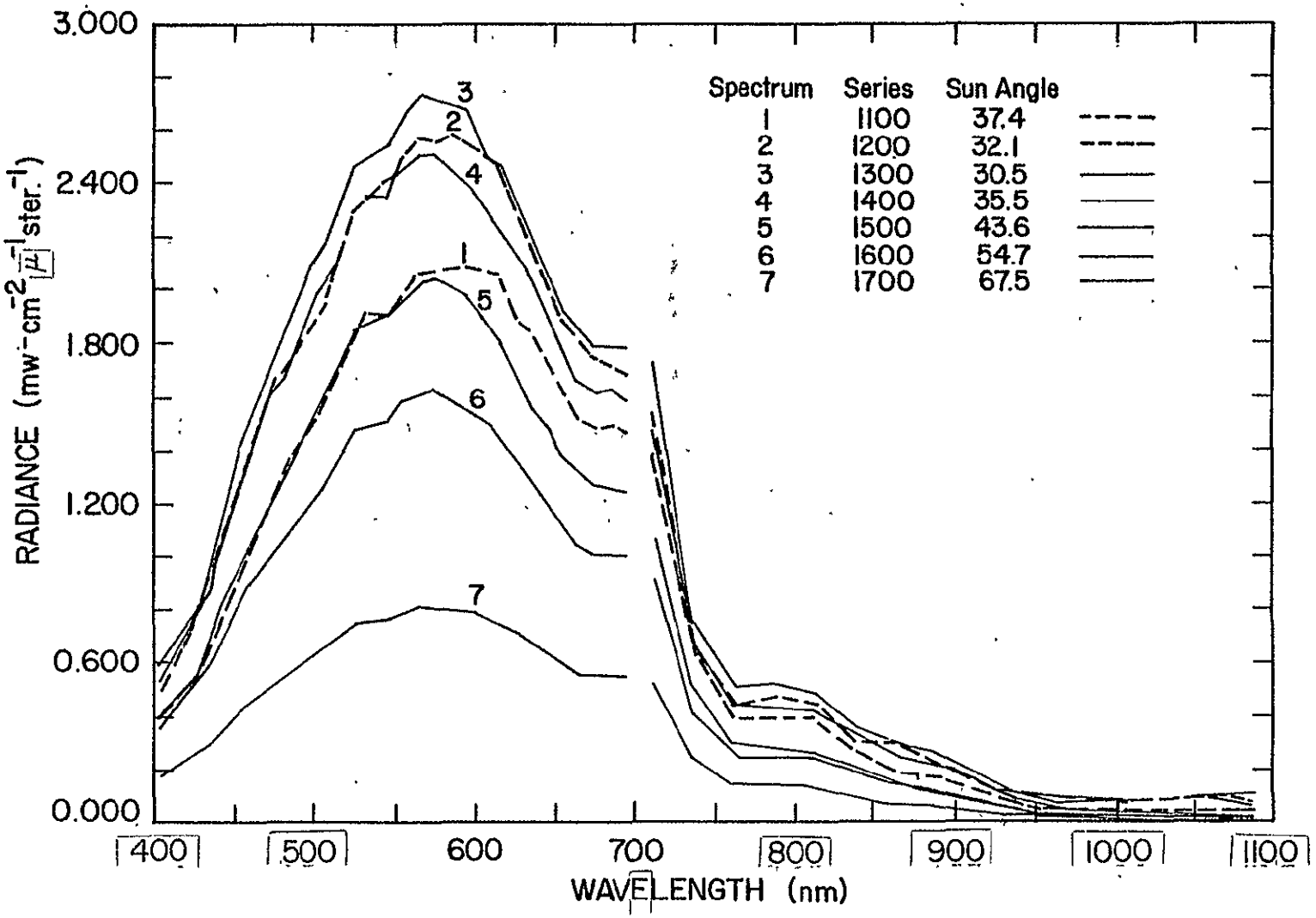

Figure 2.6 - Upwelling radiance from dockside water

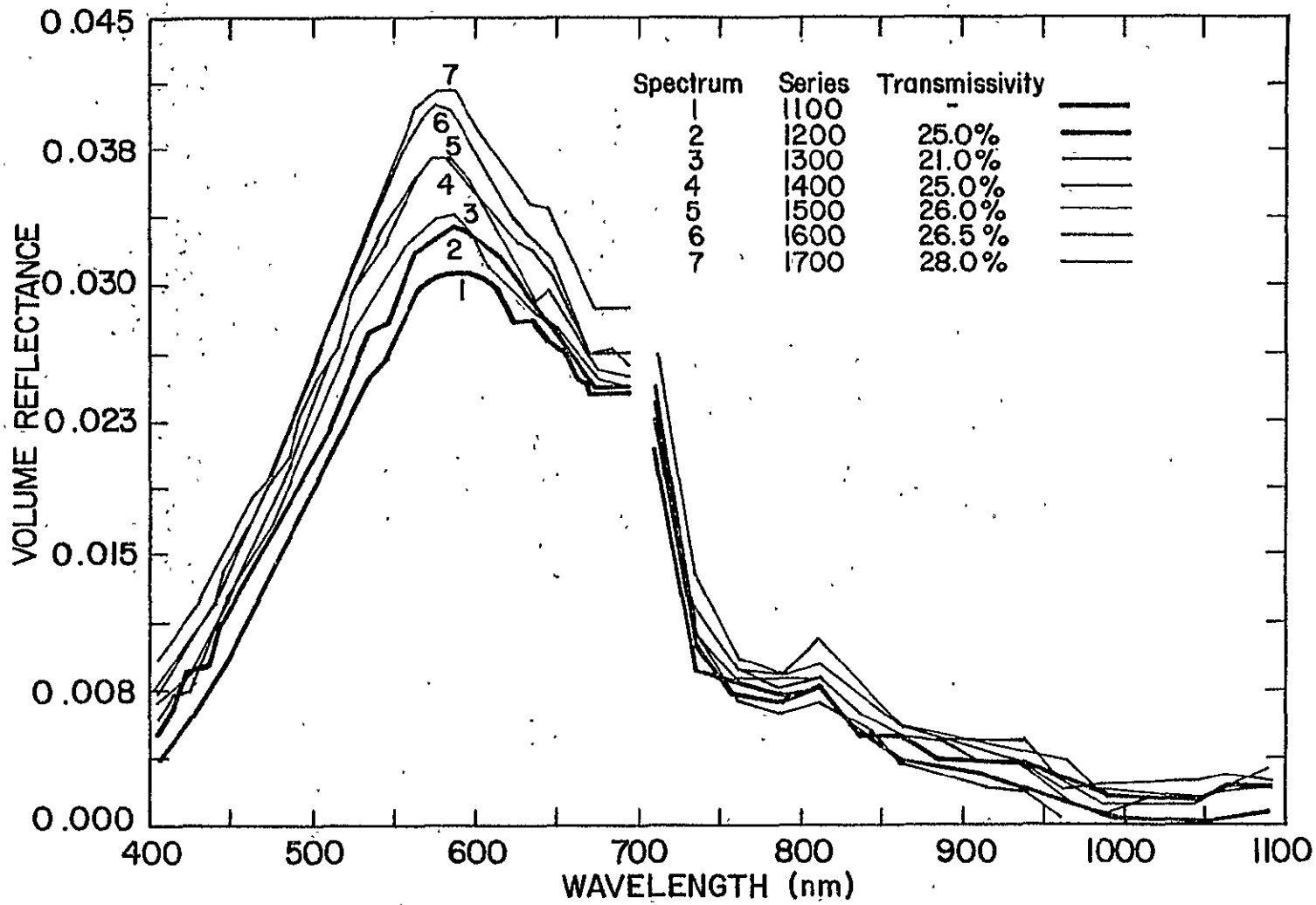

Figure 2.7 - Volume reflectance of the dock-side water.

of the upwelling spectrum due to changes in the incident light field. It is difficult to say much beyond this, however, given the obviously strong dependence on sun angle in the upwelling radiance.

The volume reflectance spectra (figure 2.7) contrast nicely to this. The dependence on sun angle is gone. Instead, the volume reflectance increases steadily with time -- hinting at a direct relation to the tidal changes in the water type.

The variability in the volume reflectance is about the same or a little lower than that for the tank data in the red portion of the spectrum (±6-8%), but increases sharply toward the blue. All of the spectra have more narrow peaks than the upwelling curves although the maxima occur in approximately the same position as before. In the area of the maxima (525-625nm) the variability in the data is about ±10% -- barely exceeding the uncertainty in the measurement itself. Strictly, this would mean that, at best, only two closely related water types were present and that these were barely distinguishable by their volume reflectance. Yet, as with the tank data, there are strong indications that much of the variability is due to the changes in the water itself.

First of all, the two spectral groups observed in the upwelling data are still clearly discernable by their shape alone in the reflectance curves. Now, however, the two groups are almost separated spatially (figure 2.7). In general, the afternoon water type appeared to be more highly reflective than the morning water type. Beyond this, the five spectra from the afternoon seem to be related to the transmissivity; as the transmissivity increases, so does the reflectance. Table 2.1 lists the transmissivity values at .5 meter intervals for each series. The transmissivity values listed in figure 2.7 are the surface values since it is the surface water that is the source of most of the return signal.

An increase in reflectance is usually related to an increase in scattering substances in the water and therefore an increase in the suspended load and a decrease in the transmissivity -- precisely the reverse of what occurs here. The transmissometer, of course, measures only the percentage of light removed from a beam of light by the water. It is impossible to tell from this measurement alone whether the light was removed by scattering or by absorption. For the transmissivity to increase at the same time that the reflectance increases implies that either absorbing material

SUN ANGLES AND REFLECTION COEFFICIENTS

SERIES	1100	1200	1300	1400	1500	1600	1700
$\theta_\odot$	37.4°	32.1°	30.5°	35.5°	43.6°	54.5°	67.5°
$\cos\theta_\odot$	.7944	.8471	.8616	.8181	.7242	.5807	.3826
$\theta'_\odot$	26.9°	23.3°	22.2°	25.4°	30.9°	37.4°	43.5°
$\rho(\theta_\odot)$	.0243	.0227	.0224	.0243	.0277	.0434	.1092

TRANSMISSIVITY

Tank	26%	26%	27%	27.5-28%	26%	24.5%	26%
dock							
surface	-	25%	21%	25%	26%	26.5%	28%
.5m	-	19%	17%	21.5%	24%	25%	29%
1.0m	-	15%	18%	20%	20.5%	21.5%	
bottom	-		18%	18%			

Time of measurements

	1115	1220	1320	1425	1525	1625	1730

Tidal data (approximate)

maximum flood - 1240

high slack - 1400

Table 2.1 - Transmissivity, reflectance coefficients, sun angles and tidal data.

is being removed directly or that the overall optical character of the water-borne substances is shifting from absorbing material to scattering material. This is essentially the explanation suggested by Hogan (1974). Hogan measured the total seston weight and transmissivity at the mouth of the Broadkill River over one tidal cycle. The mouth of the Broadkill River is about one eighth of a mile from the dock where the present experiment was conducted. Figure 2.8A illustrates Hogan's results for part of the tidal cycle. The reflectance and transmissivity data for the dockside experiment are shown for the same part of the tidal cycle in figure 2.8B. Both sets of data can best be explained by assuming that significant changes took place in the optical character of the material in the water.

Hogan's data shows a drop in the seston weight around the time of maximum flood without an attendant change in the transmissivity. This could be due to an influx of water rich in dissolved, absorbing material but relatively free of suspended matter. The total seston weight would then decrease without seriously affecting the ability of the water to remove light from the transmissometer beam because of the increase in absorption efficiency.

About one hour before slack flood both the

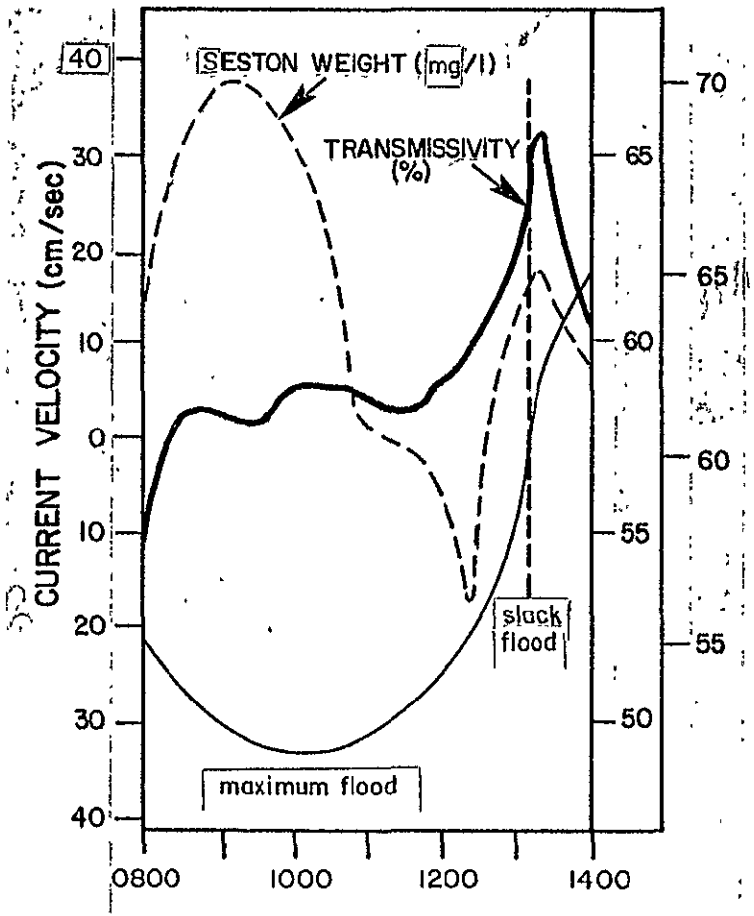

Figure 2.8A - Transmissivity and seston weight near maximum flood at the mouth of the Broadkill River. (Hogan, 1974)

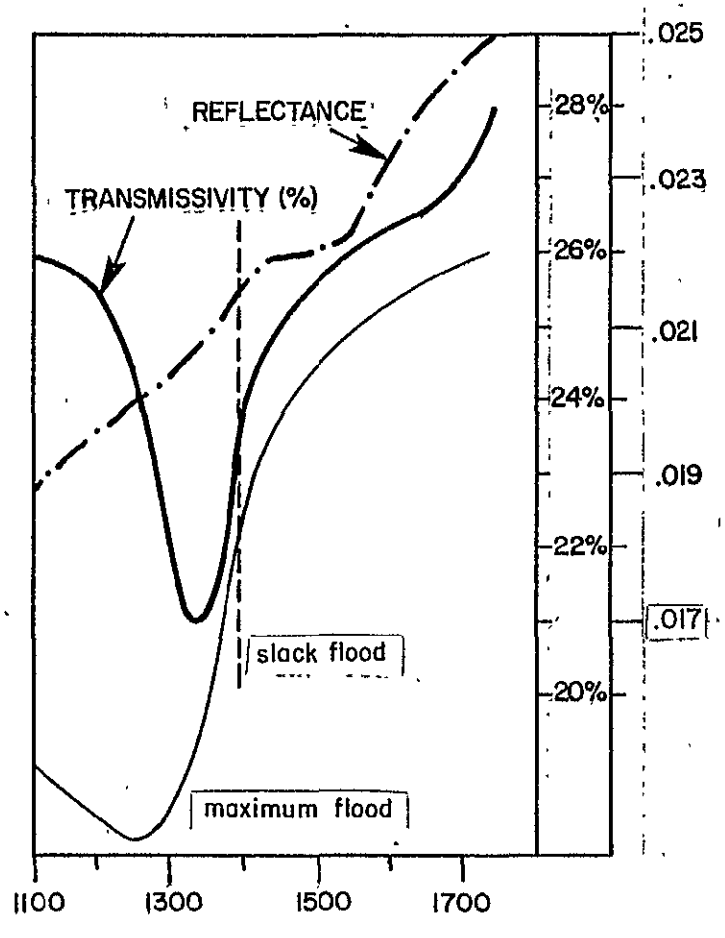

Figure 2.8B - Transmissivity and reflectance of dockside water.

transmissivity and the seston weight increased sharply. This would be best explained by a reduction in the absorbing material at the same time as an increase in smaller, denser, non-absorbing particles.

Something analogous to what is happening in Hogan's data seems to be happening in the data from the dockside experiment at the same part of the tidal cycle. Here the reflectance increases along with the transmissivity (figure 2.8B). The increase in refelctance implies an increase in the total amount of light backscattered. Increased scattering would in turn reduce the transmissivity of the water. Since the transmissivity actually increased, this implies that the absorption efficiency of the material in the water dropped drastically. The dockside data and Hogan's data both imply this loss of absorbing material or a decrease in the absorbing efficiency at about the same part of the tidal cycle.

It appears that the changes in the volume reflectance are related to real changes in the water rather than some random error in the measurement itself. There is insufficient data to actually prove that the relationship exists. However, the available evidence is very suggestive.

2.3 Summary

The passive, optical remote sensing of water quality requires a measure of water color which is sensitive to changes in the optical properties of the water but insensitive to changes in the incident light field. The volume reflectance is suggested as such a measure and is defined as the ratio of upwelling radiance to the downwelling irradiance as measured just below the water surface,

$$\rho_v = \frac{N'_u(\theta', \phi')}{H'_d}$$

The primary assumption is that, since the volume reflectance is directly related to the inherent optical properties of the water, it is itself an inherent property of the water. Insofar as the optical properties of the water are measures of the water quality, the volume reflectance should also be indicative of water quality. For a flat, homogeneous water mass of infinite optical depth, the volume reflectance is given by,

$$\rho_v = \frac{\eta^2 \left[N_u(\theta_{ob}) - \rho(\theta_{ob}) N_s(\theta_{ob}) \right]}{(1-\rho'(\theta'_{ob})) \left[2\pi N_s(.466) + (1-\rho(\theta_\odot)) \cos\theta_\odot N_\odot \Omega_\odot + 2\pi N'_u(\theta'_{ob})(.240) \right]}$$

Experiments were conducted to test the effectiveness of the volume reflectance as a measure of water quality. The results were inconclusive. The essential problem seemed to be a variability in the control -- a tank of water whose optical properties were assumed to be constant throughout the day. The variability in the control data was comparable to the variability in the dockside water which was known to vary significantly over a tidal cycle.

Upon closer inspection, the data seems to indicate that the volume reflectance is, in fact, quite sensitive to changes in the water as well as being insensitive to changes in the incident light field. But the lack of a true control and the relatively small data set make it impossible to draw any firm conclusions.

III. The Classification of Water Types Using Landsat Imagery

Landsat was not really intended for use in water observations. The gain is low, making the dynamic range of the sensor very limited over water. The four channels were selected for land use applications and are hardly ideal for water observations. Yet, there is a surprising amount of information in the Landsat imagery. Landsat data has been used to map sediment distribution patterns (Klemas et al., 1972), to observe the occurrence of estuarine fronts (Klemas and Polis, 1977) and to observe the occurrence of internal waves (Apel, 1974), to cite only a few of the many papers in which Landsat imagery has been used for water. The history of utilization, coupled with the high-probability of the continuation of the Landsat program for many years to come, is sufficient incentive for trying to extract as much as possible from the data.

One promising area of study is the use of more than one band in water analysis. Much of the work to date has been directed toward establishing a relationship between the radiance in one band and the concentration of a substance in the water (Klemas et al., 1974). Johnson (1975) used a multiple linear regression technique to relate the multispectral data to sediment concentration and showed that multi-band data can improve the correlation between the two.

There is more information in multispectral data. than is usually apparent from regression analysis. For instance, it is not immediately clear from regression analysis alone whether or not two different substances can be distinguished. What we hope to show here is that, even with low dynamic range and inappropriate spectral bands, Landsat data can be used to distinguish between different substances in the water.

Briefly, our approach is to use principal components analysis to characterize the spectral difference between "clear" and "polluted" water. The "pollutants" consist of sediment and iron-acid waste. These were the only substances in the water which could be unambiguously identified in the imagery prior to the principal components analysis. It will be shown that a sufficiently high concentration of either sediment or iron-acid waste can be distinguished from each other as well as from clouds and ice. Furthermore, classification of these targets seems to be dependent only on the identification of "clear" water. If the signature of "clear" water can be identified it may be possible to compare data from different days directly.

3.1 Iron-acid Waste

The iron-acid waste was designated for this project because it is clearly visible and easily identifiable on Landsat imagery. Over the past five years of Landsat operation, 22 satellite images have been found which exhibit water discoloration in the general vicinity of the waste dump site (Table 2.1). This discoloration can be identified as the iron-acid waste even on single-band imagery because of its location, pattern and the time between the image and the most recent dump.

Location - The waste disposal area encompasses a rectangle of five by about eight nautical miles centered approximately 38 nautical miles southeast of Cape Henlopen, Delaware (Fig. 3.1). The area is bounded on the North by 38°35'N, on the East by 74°15'W, on the South by 38°30'N and on the West by 74°24'W. The water depth throughout the area is between 38 and 45m.

Table 3.1. Landsat Imagery of Iron-Acid Waste.

	Overpass Date	ID Number	Time After Dump Completion
1)	10 OCT 72	1079-15133	9 hrs 38 min
2)	27 OCT 72		14 hrs 8 min
3)	25 JAN 73	1186-15081	3 hrs 3 min
4)	7 APR 73	1258-15085	6 hrs 38 min
5)	13 MAY 73	1294-15083	During Dump
6)	22 OCT 73	1456-15055	29 hrs 30 min
7)	23 OCT 73	1457-15113	53 hrs 36 min
8)	15 DEC 73		4 hrs 45 min
9)	15 MAR 74	1600-15031	6 hrs 8 min
10)	20 APR 74	1636-15031	13 hrs 47 min
11)	26 MAY 74	1672-15012	22 hrs 1 min
12)	4 NOV 74	1834-14561	12 hrs 26 min
13)	19 AUG 75	5122-14420	During Dump
14)	28 AUG 75	2218-14552	5 min
15)	21 OCT 75	2272-15004	1 hrs 55 min
16)	17 NOV 75	5212-14364	2 hrs 41 min
17)	19 JAN 76	2362-14540	39 min
18)	24 FEB 76	2398-14531	3 hrs 23 min
19)	18 APR 76	2452-14513	70 hrs 19 min
20)	20 JUN 76		
21)	17 JUL 76		
22)	22 AUG 76	2578-14481	

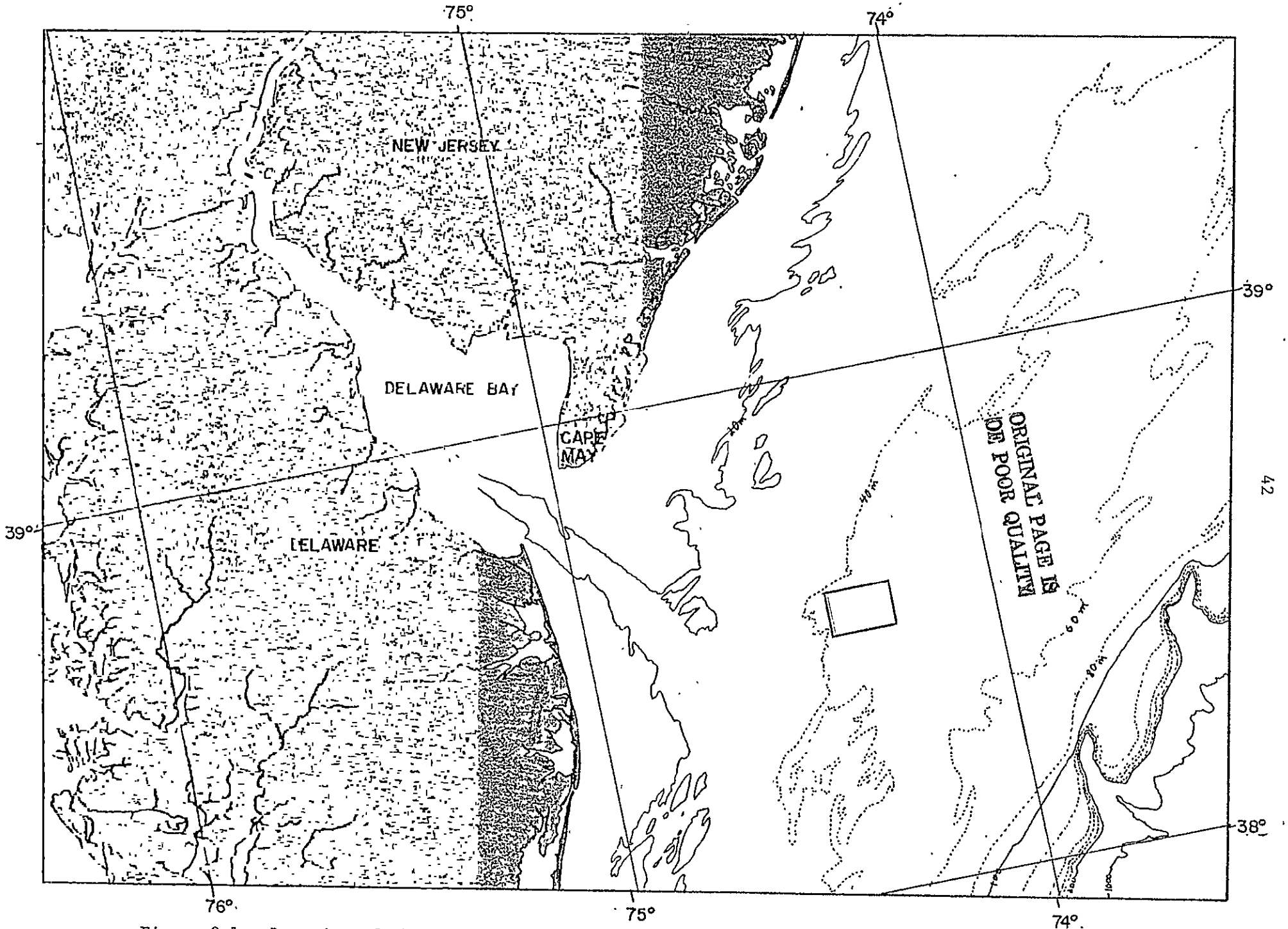

Figure 3.1. Location of the iron-acid waste dumpsite.

Pattern - Until May 1974 the discharge time was usually about 60 minutes at a speed of 6 knots, weather and other conditions permitting. The waste at this time was 17% to 23% acid (expressed as H_2SO_4) and 4% to 10% ferrous sulfate. The typical dump pattern during this period resembled a fish-hook as in the Landsat image for 25 January 1973 (Figure 3.2). After May 1974 the discharge time was increased to about five hours at a speed of eight knots and the composition of the waste changed to 10% acid (expressed as HCl) and 4% iron chloride salts. The pattern of dumping was also altered in order to spread a more diluted form of the waste over the largest permissable area. The new pattern resembled a bow tie or figure eight as can be seen on the Landsat image for 28 August 1975 (Figure 3.3).

Time After Dump - Both of the above examples were shortly after the dump was completed. Thus the patterns were complete, undistorted and squarely in the dumpsite area. In several cases, however, the overpasses occurred either during dumping or sufficiently long after dump that the dump pattern was not easily recognizable. Thus, whenever a pattern was seen on the imagery in the general area of the dumpsite which was suspected of being a waste plume, the dump records* were checked to verify whether or not this was the dump. In most cases the combination of the dump records with the location and pattern of a feature on the imagery was sufficient for positive identification.

Purely visual observation, however, is inadequate on days when the dump pattern is partially obscured by clouds and/or haze. Identification of a dump may also be hindered by the presence of other particulate and

*The dump records were provided by E. I. duPont de Nemours and Co., Inc.

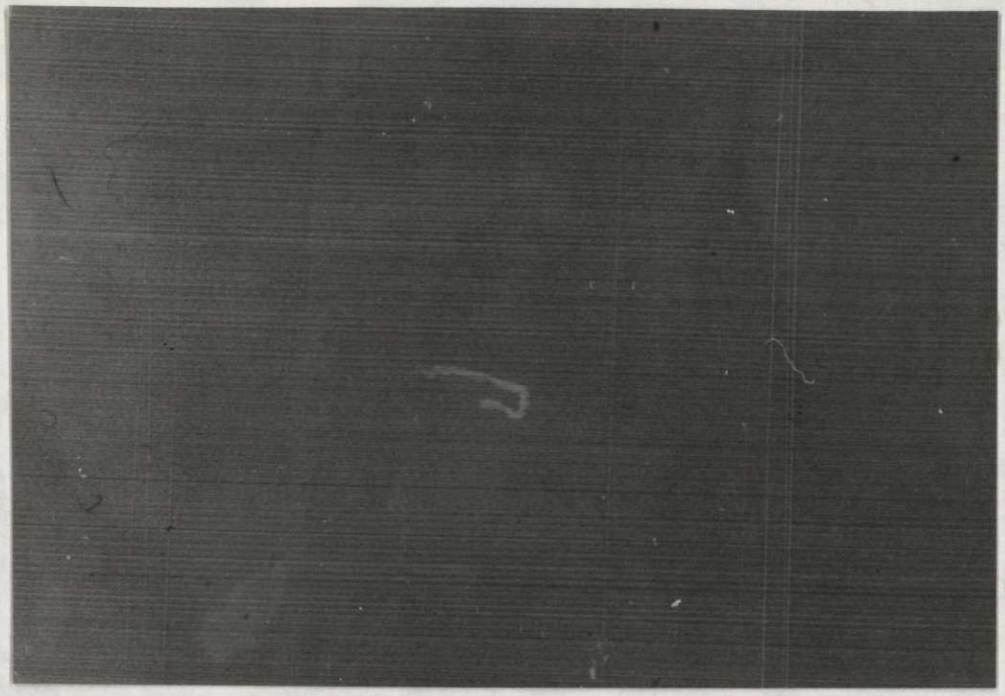

Figure 3.2. Landsat - 25 January 1973.

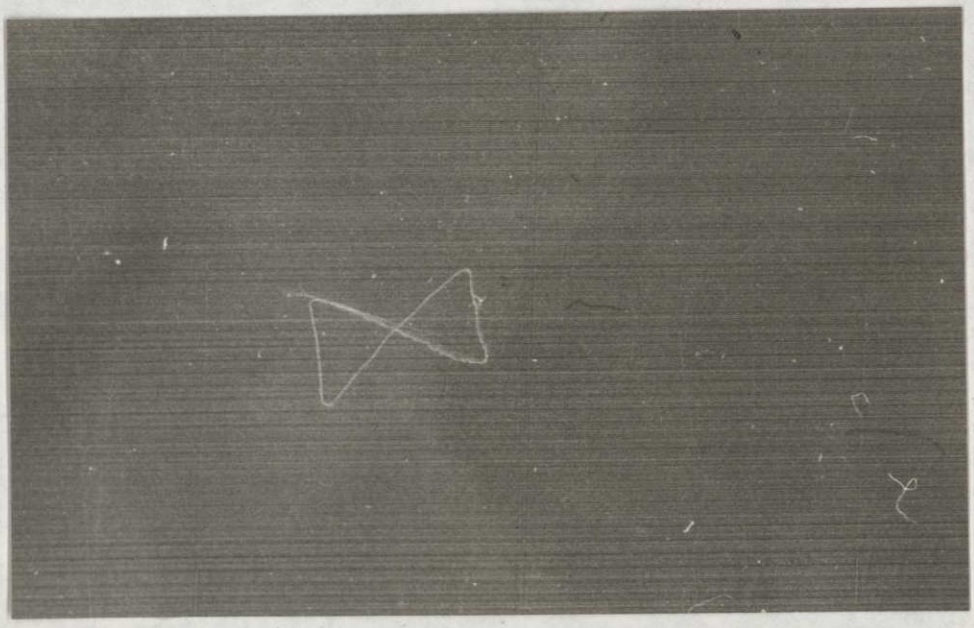

Figure 3.3. Landsat - 28 August 1975.

dissolved matter in the adjacent waters. What we seek, then, is a means of positively identifying this and/or other substances by the spectral reflectance characteristics as viewed from Landsat.

3.2 Principal Components Analysis

Spectral data can be rather awkward to deal with. In the present case one is faced with the task of simultaneously observing variations in four bands, not the easiest of tasks. Displaying the spectra as a family of curves helps considerably in visualizing the problem but often aids surprisingly little in solving it, especially in quantitative terms. Statistical analyses, on the other hand, while facilitating quantitative analysis of the data, are often difficult to conceptualize. In this case the data needs no aid in being difficult to conceptualize. Indeed, it is fairly important that the statistical approach aid in both the data reduction and the conceptualization of the problem.

The statistical procedure chosen is that of eigenvector analysis, a fairly common method with data of this sort. The use of principal components analysis in studies of ocean color was first undertaken by Mueller (1976), in his study of phytoplankton. Mueller's work was a classic application of the technique and demonstrated the effectiveness of eigenvector analysis in analyzing water color spectra. The derivation of eigenvector analysis will not be covered here, since it is covered in detail in several sources [see Morrison (1976]. The method, does, however, lend itself to a geometrical interpretation which aids considerably in understanding the results.

First let us consider the problem in two dimensional form. Suppose that we are viewing a water scene which includes a dye or pollution

plume with a two-band scanner. Each pixel in the scene could be plotted according to its intensity values in the two bands (Figure 3.4). Since the spectral characteristics of water vary continuously over a rather narrow range, the set of pixels is likely to plot out as some sort of ellipsoid. The major axis of the ellipsoid (B'_1) is along the direction of maximum variance. The remaining variance in this two-dimensional system is accounted for by the minor axis (B'_2). If the ellipsoid is quite eccentric, as might be the case if the scene covered a "bright" dye or pollutant in clear water, the vast majority of the variance would occur along the direction of the major axis. In this case the displacement of a point along the direction of the major axis (denoted as Y_1 in Figure 3.4) would probably correlate with the concentration of the dye or pollutant in the water. The correlation would be carried out using the concentration as the independent variable and the magnitude Y_1 as the dependent variable. The correlation itself may be linear or non-linear although Y_1 is always a linear combination of the two original variates B_1 and B_2.

An important point here is that, even in this simple, two-dimensional system the number of significant variates has been reduced. The results can be far more dramatic in a multi-dimensional system. It is quite reasonable to expect that water spectra in general may be represented effectively by a system of three or four variates however finely the spectrum is broken down (Mueller, 1976).

Eigenvector Analysis is nothing more than the method of calculating these variates by translation and rotation of the original coordinate system. The new system of variates form an orthoganal set of which the

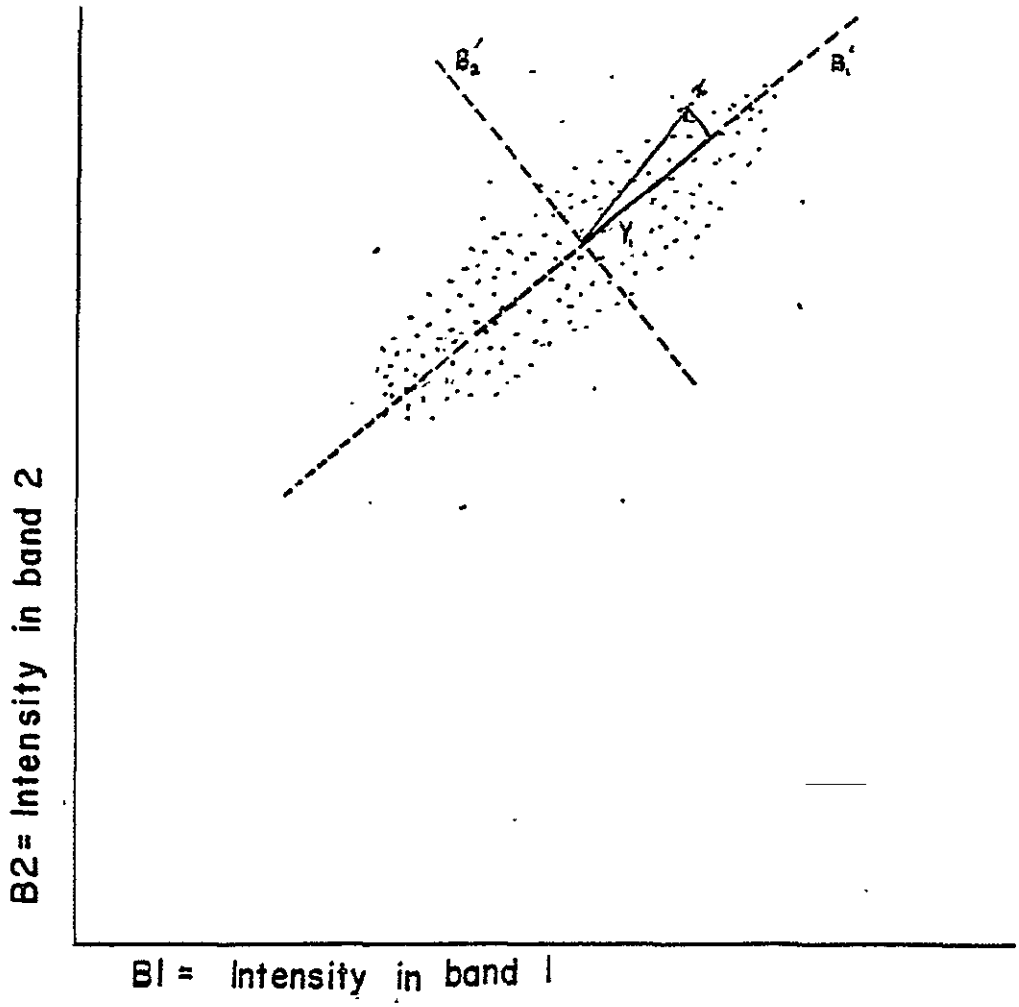

FIGURE 3.4. Two-band intensity plot

first eigenvector (principal component) is in the "direction" of maximum variance, the second eigenvector is in the "direction" which maximizes the remaining variance, and so on.

3.2.1 Calculation of Principal Components

This section is not essential to understanding the results. It is included to facilitate use of this method in further studies.

Principal Component = eigenvector = characteristic vector

Characteristic root = eigenvalue = characteristic value

Suppose we have n data points from a p-band scanner. This data can be put in the form of a data matrix W where each row corresponds to an individual sample, and each column corresponds to an individual band.

$$W = \begin{pmatrix} \omega_{11} & \omega_{12} & \cdots & \omega_{1j} & \cdots & \omega_{1p} \\ \omega_{21} & & & & & \\ \vdots & & & \vdots & & \vdots \\ \omega_{i1} & \cdots & \cdots & \omega_{ij} & & \\ \vdots & & & & & \\ \omega_{n1} & \cdots & \cdots & \cdots & \cdots & \omega_{np} \end{pmatrix} \quad \begin{matrix} i = 1, n \\ n = \text{total number of spectra} \\ j = 1, p \\ p = \text{total number of bands} \end{matrix} \qquad (3.1)$$

The mean spectrum is simply the average value of the columns

$$\bar{R} = (R_1, R_2, \ldots R_p) \qquad R_j = \sum_{i=1}^{n} \omega_{ij} \qquad (3.2)$$

Consider for the moment, a three band scanner. If we consider a coordinate system in which each band corresponds to one axis and the intensity in that band is related to the distance along that axis then all the spectral data can be plotted as a distribution of points in this three-dimensional space and $\bar{R}$ is the vector from the origin to the mean spectrum. The first step of the computation is to translate the coordinate system so that the new origin is at the mean spectrum. This is accomplished by subtracting the mean spectrum from each spectrum in the data matrix. The result is the mean corrected data matrix P.

$$P = \begin{pmatrix} \omega_{11} - R_1 & \omega_{12} - R_2 & \cdots & \omega_{1j} - R_j & \cdots & \omega_{1p} - R_p \\ \omega_{21} - R_1 & & & & & \\ \vdots & & & & & \\ \omega_{i1} - R_1 & \cdots & \cdots & \omega_{ij} - R_j & & \\ \vdots & & & & & \\ \omega_{n1} - R_1 & \cdots & \cdots & \cdots & \cdots & \omega_{np} - R_p \end{pmatrix} \tag{3.3}$$

and,

$$P_{ij} = \omega_{ij} - R_j \tag{3.4}$$

Next we must rotate the coordinate system so that one axis points along the direction of maximum variance. In Figure 3.5 this direction is represented by $\hat{a}_1$ which is along the major axis of the ellipsoid. The vector $\hat{a}_1$ will be the first principal component. In order to carry out this rotation we must first form the covariance matrix. This is done quite simply by premultiplying P by its transpose. Explicitly,

$$P^T P = \begin{pmatrix} \omega_{11} - R_1 & \cdots & \omega_{m1} - R_1 \\ \vdots & & \vdots \\ \omega_{1p} - R_p & \cdots & \omega_{np} - R_p \end{pmatrix} \begin{pmatrix} \omega_{11} - R_1 & \cdots & \omega_{1p} - R_p \\ \vdots & & \vdots \\ \omega_{n1} - R_1 & \cdots & \omega_{np} - R_p \end{pmatrix} \tag{3.5}$$

For each element of $P^T P$ we have

$$(P^T P)_{11} = (\omega_{11} - R_1)^2 + (\omega_{21} - R_1)^2 + \cdots + (\omega_{n-1} - R_1)^2 \tag{3.6}$$

$$(P^T P)_{12} = (P^T P)_{21} = (\omega_{11} - R_1)(\omega_{12} - R_2) + (\omega_{21} - R_1)(\omega_{22} - R_2) + \cdots + (\omega_{n-1} - R_1)(\omega_{n2} - R_2) \tag{3.7}$$

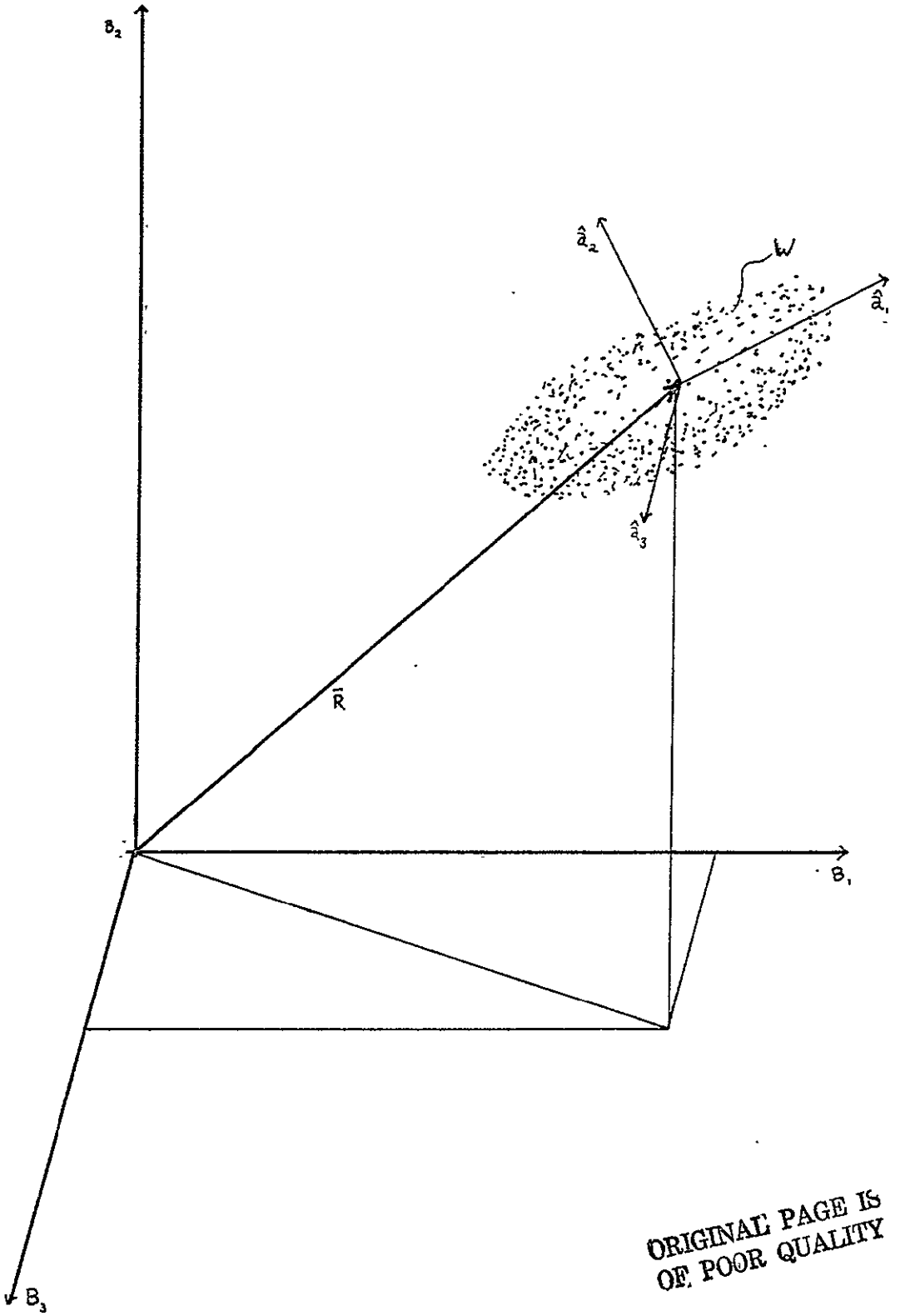

Figure 3.5.

or in general:

$$\left(P^T P\right)_{jk} = \sum_{i=1}^{n} \left(\omega_{ij} - R_j\right)\left(\omega_{ik} - R_k\right) = \left(P^T P\right)_{kj} \tag{3.8}$$

If this value is divided by $(n-1)$ it is exactly the expression for covariance between bands j and k.

Along the diagonal where j=k then:

$$\left(P^T P\right)_{jj} = \sum_{i=1}^{n} \left(\omega_{ij} - R_j\right)^2 = (n-1)\sigma^2 \tag{3.9}$$

where σ^2 = variance along band j (original coordinate system).

The covariance matrix estimate A is actually given by

$$S = \frac{1}{n-1}\left(P^T P\right) \tag{3.10}$$

This further division is not actually carried out since it does not change the results at all. $P^T P$, then, is a square (pxp) matrix, with the variance in each band related directly to the values along the diagonal and the covariance between bands related directly to the off-diagonal elements.

The trace of S is equal to the total system variance:

$$tr\, S = \left(\frac{1}{n-1}\right) tr\left(P^T P\right) = \sum_{j=1}^{p} \left(P^T P\right)_{jj} \tag{3.11}$$

*If the eigenvalues (characteristic roots) λ_i of S are ordered by their absolute values:

$$|\lambda_1| > |\lambda_2| \geq \cdots\cdots |\lambda_p| \tag{3.12}$$

and their respective eigenvectors (characteristic vectors) are denoted as

*Much of the following is taken directly from Morrison (1976).

$$\hat{a}_1, \hat{a}_2, \hat{a}_3, \hat{a}_4, \ldots, \hat{a}_p \tag{3.13}$$

then we may form the sequence

$$\begin{aligned} \bar{x}_1 &= S\bar{x}_0 \\ \bar{x}_2 &= S\bar{x}_1 \\ &\vdots \\ \bar{x}_n &= S\bar{x}_{n-1} \end{aligned} \tag{3.14}$$

where $\bar{x}_0$ is <u>any</u> vector of p real components. Then if the successive x_i are scaled in some fashion the sequence of standardized vectors will converge to the eigenvector $\hat{a}_1$. Probably the most convenient and efficient scaling is performed by dividing the components by their maximum value, with normalization to unit length reserved for the last, or exact vector. The demonstration of this convergence is given by Morrison (1976). This is precisely the method described by Simmonds (1963)

Since
$$S\hat{a}_i = \lambda_i \hat{a}_i \tag{3.15}$$

the eigenvalue (characteristic root) itself can be found by dividing any element of $A\hat{a}_1$ by the corresponding element of $\hat{a}_1$. The eigenvalue is numerically equivalent to the amount of variance accounted for by the associated eigenvector. Thus, recalling that the trace of S is the total system variance, we have

$$\lambda_1 + \lambda_2 + \cdots + \lambda_p = tr\, S = \left(\frac{1}{n-1}\right) tr\, A \tag{3.16}$$

and the percentage of the variance acounted for by the jth eigenvector is given by:

$$\lambda_j / tr\, S = \%\ \text{variance accounted for by } \hat{a}_j \tag{3.17}$$

There is a slightly more efficient procedure for calculating the principal components which is presented by Morrison (1976). From equation (3.14) it can easily be seen that

$$\bar{x}_n = S^n \bar{x}_o \tag{3.18}$$

In other words, where Simmonds' procedure calculates each successive x_i until the sequence converges, Morrison calculates powers of the covariance matrix. For distinct eigenvalues, that is, when x_i is significantly greater than λ_{i+1} both methods are equivalent. However, when λ_i and λ_{i+1} are more nearly equal and convergence is slow, the matrix-power method is a considerable improvement in calculation efficiency.

The same iterative procedure can be used to compute any distinct characteristic root of A. To extract the second largest root and its vector we form the pxp matrix

$$\lambda_1 \hat{a}_1 \hat{a}_1' \tag{3.19}$$

and subtract it from A to give the residual matrix

$$A_1 = A - \lambda_1 \hat{a}_1 \hat{a}_1' \tag{3.20}$$

Here the primed vectors are row vectors and unprimed vectors are column vectors.

To summarize:

1). Form the data matrix W_{ij} where

i = 1,n; n = total number of samples

j = 1,p; m = total number of bands

2). Calculate the average, or mean spectrum R_j:

$$R_j = \frac{1}{n} \sum_{i=1}^{n} \omega_{ij}$$

3). Form the Mean-Corrected Data Matrix P_{ij}:

$$P_{ij} = W_{ij} - R_j$$

4). Find the transpose of P_{ij} and create the covariance matrix S by premultiplying P_{ij} by its transpose.

$$A_{ij} = P_{ij}^{T} P_{ij} \quad (= P_{ji} P_{ij})$$

$$S_{ij} = \left(\frac{1}{n-1}\right) A_{ij}$$

There is no need to calculate S explicitly since A suffices for the calculations.

5). Take the square of A and multiply A^2 by a column vector of ones (or premultiply it by a row vector of ones) to find the first estimate of first eigenvector:

$$\bar{X}_2 = A^2 \bar{X}_0 = \bar{X}_0' A^2$$

where $\bar{X}_0' = (1,1,1,\ldots,1)$

6). Normalize $\bar{x}_2$ by dividing each element of the vector by the largest element:

$$\frac{\bar{X}_2}{X_{2\,max}}$$

7). Find the next power of A and multiply that by a column vector of ones to get the second estimate of the first eigenvector:

$$\bar{X}_4 = A^4 \bar{X}_0 = \bar{X}_0' A^4$$

8). Normalize $\bar{x}_4$ by dividing each element by the maximum value and compare $|x_2|$ and $|x_4|$.

$$\lim_{+} > |\bar{X}_2| - |\bar{X}_4| > \lim_{-}$$

where lim is a value chosen depending on the accuracy required. For most purposes $lim_+ = 0.0001$ is sufficient. If the values are sufficiently close then keep $\bar{x}_4$ as the best estimate of the first eigenvector. If the magnitudes of these two estimates are not within this limit, continue calculating powers of A and the resulting eigenvector estimate:

$$\bar{X}_n = A^n \bar{x}_o$$

until the condition is met that:

$$lim_+ > |\bar{x}_n| - |\bar{x}_{n-1}| > lim_-$$

9). Having chosen $\bar{x}_n$ as the best estimate of the eigenvector, it should be normalized to a unit vector. Thus the eigenvector $\hat{a}_1$ is given by:

$$\hat{a}_1 = \frac{\bar{x}_n}{\sqrt{\sum_{i=1}^{p} (x_i)^2}}$$

10). The associated eigenvalue , is given by (characteristic root)

$$l_1 = \sum_{i=1}^{p} \frac{\hat{a}_i}{\hat{a}_1} A_{1i} \qquad \text{where} \quad \hat{a}_1 = (a_1, a_2, a_3, \ldots, a_p)$$

The true eigenvalue, λ_1, and thus the variance accounted for by the first eigenvector, must be calculated from the actual covariance matrix, therefore:

$$\lambda_1 = \sum_{i=1}^{p} \frac{\hat{a}_i}{\hat{a}_1} S_{1i} = \frac{1}{n-1} \sum_{i=1}^{p} \frac{\hat{a}_i}{\hat{a}_1} A_{1i}$$

$$= \frac{l_1}{n-1}$$

11). The percent of total variance accounted for by the first eigenvector is given by

$$\text{Percent of total variance} = \frac{\lambda_1}{tr\, S} = \frac{\ell_1}{tr\, A}$$

Since the latter is more efficient to calculate, neither λ_1 nor S is actually calculated exactly. Instead, ℓ_1 and A are used with no loss in precision. Indeed, there is even a gain in precision since calculation of S would include additional round-off errors.

12). The residual covariance matrix is calculated by

$$S_1 = S - \lambda_1 \hat{a}_1 \hat{a}_1'$$

or equivalently

$$A_1 = A - \ell_1 \hat{a}_1 \hat{a}_1'$$

where again the prime indicates a row vector.

If further eigenvectors are needed, the same iterative procedure can be used based on the residual covariance matrix. Remembering that the trace of S is the total amount of variance in the system and

$$\lambda_1 + \lambda_2 + \ldots + \lambda_p = tr\, S$$

and

$$\ell_1 + \ell_2 + \ldots + \ell_p = tr\, A$$

it is easily seen that the percent of variance accounted for by the j^{th} eigenvector is simply

$$\frac{\ell_j}{tr\, A} = \frac{\lambda_j}{tr\, S} = \%\ \text{variance accounted for by } a_j$$

It is important to remember that, unless a substantial number of decimal places are carried along in the computations, the accumulation of round-off error tends to make extraction of smaller roots and their vectors difficult. This is particularly true if the roots are close in value, for the iterative process may alternately approximate one vector and then the other without converging.

3.3 Application of Eigenvector Analysis to Landsat Data

The first step in eigenvector analysis is the calculation of the mean spectrum, the average value of all the data to be used in the analysis. Since data from several different overpasses are being compared this would require correcting each days data for atmospheric effects before performing the analysis. This is not practicable at present.

One alternative is to choose the spectrum of "clear" water as the origin. This approach is roughly equivalent to using a reflectance standard against which all other targets are compared and presumes that "clear" water is present in each scene and that the atmospheric effects are essentially constant over the area of interest. The restriction of having clear water standard in each scene could easily be removed if a viable atmospheric correction technique is found, in which case a clear water standard could be calculated.

Choosing a "clear" water standard, however it is done, has important implications in the use of principal components. Conceptually, this choice assumes that the "clear" water standard forms a base spectrum and that the addition of other material to the water will cause a deviation from that base -- different materials may cause deviations in different directions but they should both be radially outward from the base. This is illustrated in Figure 3.6 where the two distributions can be characterized by vectors $\vec{A}$ and $\vec{B}$ with their origin at 0. As long as the standard spectrum corresponds to point 0, the principal components analysis will be a useful tool. If on the other hand the standard should fall at point 0', then principal components analysis (relative to this point) will gain nothing. Intuitively, it seems reasonable to assume that clear water

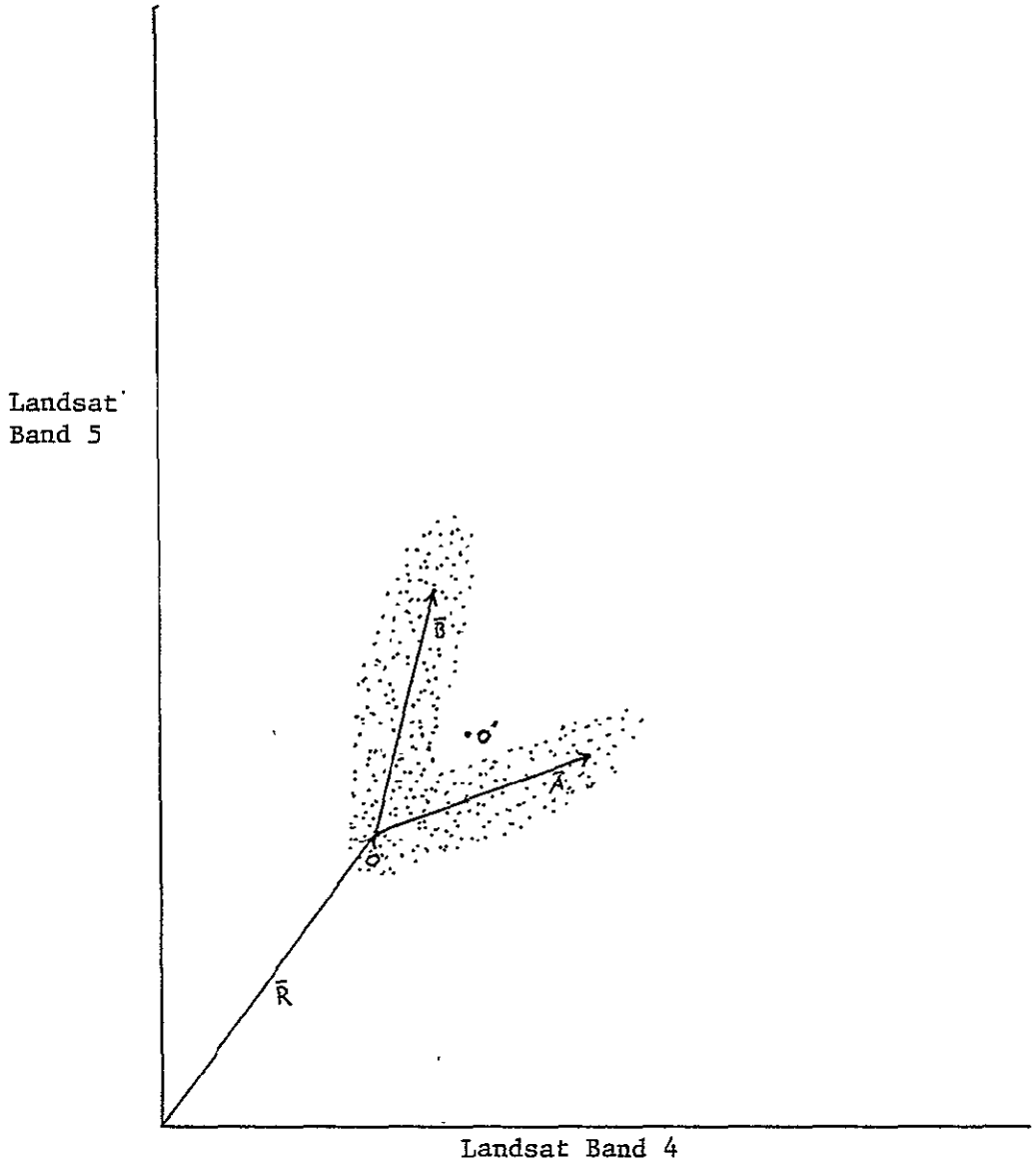

Figure 3.6. Diagram of the geometry of the eigenvector analysis. The origin has been placed at the position of the "clear" water standard.

would meet the above criterion. Clear water will have a certain signature. Addition of any material to the clear water will cause that signature to deviate from the clear water signature -- the more material added, the greater the deviation.

3.3.1 Procedure

Six Landsat scenes were chosen for the initial trial. Figures 3.7 through 3.12 show the scenes. In each case the iron-acid waste dumpsite area is shown as an insert. The areas marked on the inserts are the locations of the training sets. The training set for water (training set 1) was examined first and the mean value of the counts in each band was calculated. These values, listed in Table 3.2, were then used as the mean spectrum R_j in the components analysis. Some of the variability in the clear water means on different days (the R_j's in Table 3.2) is due to differences in atmospheric conditions. Some, however, is simply an artifcat of the gain and offset settings on the satellites. The higher values for the R_j's (17 November 1975, 19 August 1975, and 15 March 1974) are all from Landsat-1 while the lower values were from Landsat-2. The variability is reduced somewhat if one considers radiance rather than the raw counts, with the notable exception of the data on 19 August 1975 which was a particulary hazy day (see Figure 3.11). The eigenvector analysis was carried out using counts since we did not originally expect to compare data from different days directly. Direct comparison of different days should be done in terms of radiance; the use of counts will introduce some error into the results, although it will probably not be terribly significant since all the values used in the computations are relative to the clear water standards.

Table 3.2. Clear water training sets.

Date	Tape ID	Training Set	First Pixel	First Scan Line	Last Pixel	Last Scan Line	# of Pts.	Band (j)	(R_j) Mean (counts)	Std. Dev.	Mean Radiance (mw/cm^2)
24 FEB 76	2398-14531 Landsat-2	7	700	1500	740	1505	246	4	8.26	.80	.251
								5	4.91	.73	.128
								6	1.18	.94	.074
								7	0.02	.13	.111
19 JAN 76	2362-14540 Landsat-2		535	1385	550	1396	192	4	7.44	.64	.234
								5	4.58	.73	.123
								6	0.99	.83	.072
								7	0	0	.110
17 NOV 75	5212-14364 Landsat-1	1	660	1800	680	1811	252	4	14.11	.77	.276
								5	6.22	.66	.098
								6	3.02	.54	.042
								7	0.21	.41	.041
21 OCT 75	2272-14550 Landsat-2		475	1623	486	1630	96	4	9.45	.52	.276
								5	5.97	.83	.143
								6	1.81	.76	.082
								7	0	0	.110
19 AUG 75	5122-14420 Landsat-1		701	1796	710	1807	120	4	22.38	.96	.437
								5	10.88	.62	.171
								6	5.97	.72	.083
								7	0.86	.56	.054
15 MAR 75	1600-15021 Landsat-1		579	1854	587	1871	162	4	16.19	.72	.316
								5	7.10	.51	.112
								6	3.20	.62	.004
								7	0.40	.49	.025

Figure 3.7. Landsat image for 24 February 1976. The insert shows the acid plume and the sites of the training sets.

Figure 3.8. Landsat image for 19 January 1976.

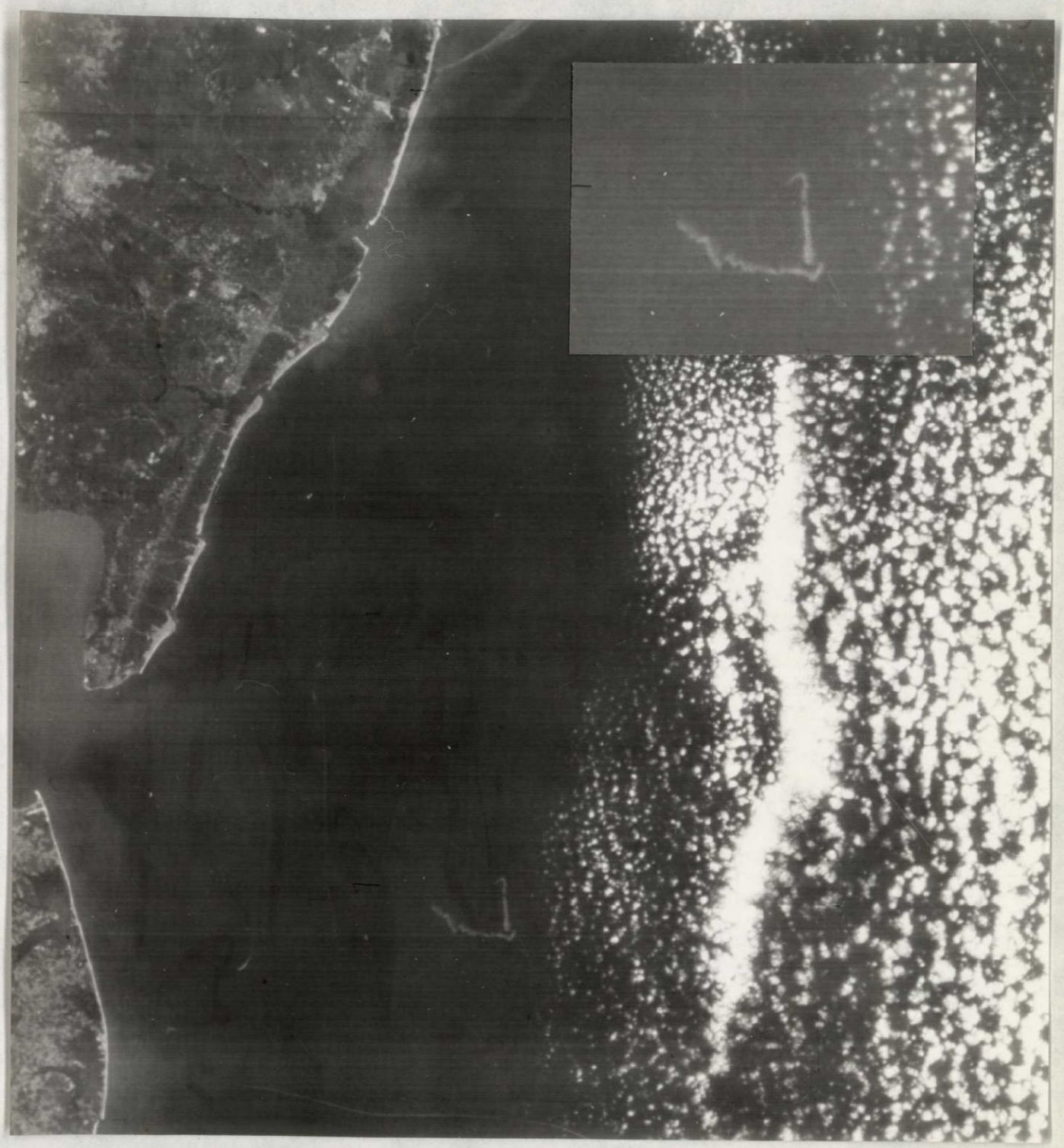

Figure 3.9. Landsat image for 17 November 1975.

Figure 3.10. Landsat image for 21 October 1975.

Figure 3.11. Landsat image for 19 August 1975.

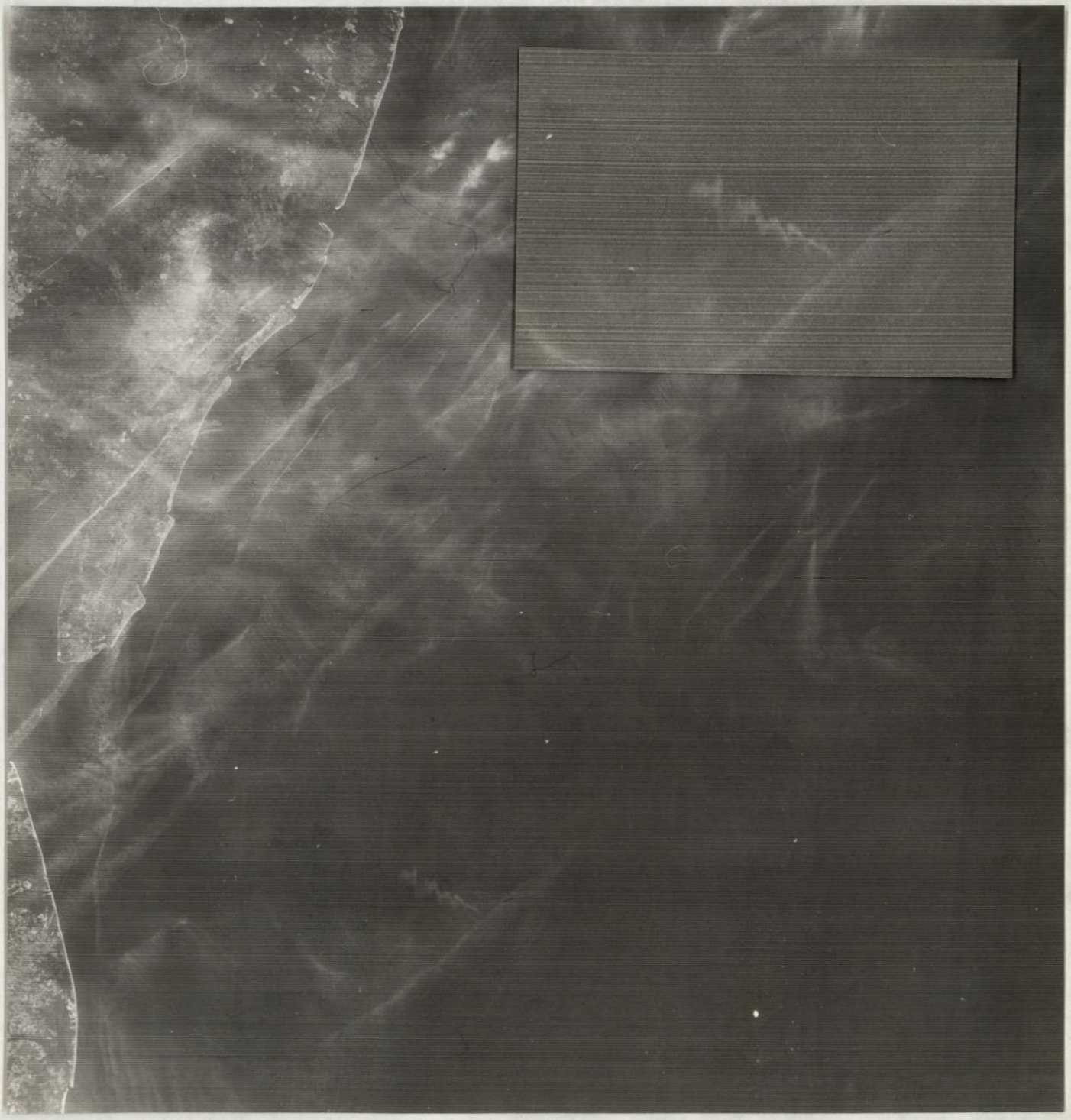

Figure 3.12. Landsat image for 15 March 1974.

The next step is to perform the eigenvector anlaysis. The data base which is calculated from the associated eigenvalue using equation 3.17 always included the "clear" water data and all the data in the training sets for one target. On days such as 19 January 1976, where all four targets (acid, sediment, clouds, and ice) were present, the analysis was performed on each target data set separately. As described earlier, the analysis yields the set of vectors which most efficiently accounts for the variance in the data. These vectors are listed in Table 3.3. Note that the first two vectors alone account for better than 90% of the variance in most cases.

Also listed in Table 3.3 are the standard deviations of the data along each eigenvector, σ_i. If, as we have been assuming, the data cluster actually forms an ellipsoid, then the first eigenvector accounts for most of the variance in the data due to real changes in the target, and the variation along the second eigenvector is primarily random noise. In this simple case, σ_2 is a measure of the dispersion of the data about the first eigenvector, and the ratio of σ_2 to σ_1 is a measure of the eccentricity of the ellipsoid.

We now have enough parameters to describe the typical distribution of pts. relative to "clear" water for several targets. The next step is to use this information as the basis for a classification scheme. We must be able to take pixel from the Landsat data and decide which of the classes, if any, that it belongs to. Figure 3.13 illustrates the problem for a two-band system. In this figure we have three classes whose first eigenvectors are $\hat{a}$, $\hat{a}'$, and $\hat{a}''$. The dotted lines parallel to the first eigenvectors represent the dispersion of data about the axis and can be characterized by the standard deviation ($\sigma_{\hat{a}_2}$) of the training data along the direction of the second eigenvector ($\hat{a}_2$). For illustration we

Table 3.3. Eigenvectors and associated standard deviations.

	Date	Eigen-vector $\hat{a}_i$	Band 4	Band 5	Band 6	Band 7	% Var. Accounted For	Std. Dev. σ_i
ACID	24 FEB 76	i = 1	.89006	.45326	.04844	.00128	77.4	1.58
		2	.03924	-.18204	.98251	-.00080	13.4	0.78
		3	-.45415	.87258	.17982	.00507	9.0	0.64
		4	.00119	-.00515	-.00019	.99999	0.1	0.08
	19 JAN 76	1	.80625	.52433	.27370	.01103	83.7	1.88
		2	-.18024	-.22318	.95784	.01579	9.9	0.73
		3	-.56344	.82165	.08522	.01245	6.3	0.58
		4	--	--	--	--	--	--
	17 NOV 75	1	.91054	.40097	.09976	.01347	92.9	2.69
		2	-.41207	.89273	.17813	-.03887	3.8	0.64
		3	-.01039	-.20459	.94931	-.23844	2.1	0.48
		4	-.03170	-.02008	.23903	.97029	1.1	0.35
	21 OCT 75	1	.85815	.51174	.04117	0	88.7	2.27
		2	.10751	-.25756	.96026	0	6.8	0.74
		3	-.50201	.81962	.27604	0	4.5	0.60
		4	--	--	--	--	--	--
	19 AUG 75	1	.78774	.58507	.18929	.03636	94.0	4.31
		2	-.59234	.80188	-.02752	.07328	4.0	1.01
		3	-.16428	-.06016	.93113	-.32000	1.4	0.60
		4	-.04005	-.10519	.31051	.94388	0.6	0.41
	15 MAR 74	1	.89507	.41904	.15020	.02640	91.9	2.61
		2	-.44435	.82057	.33648	.12648	3.6	0.64
		3	.00886	-.32879	.90932	-.25487	3.1	0.59
		4	.03635	-.20729	.19329	.95831	1.4	0.40
	AVERAGE	1	.85797	.48240	.13376	.01476		
		2	[No clear directional preference]					
		3						
		4	.00730	-.08443	.16566	.96812		

	Date	Eigen-vector $\hat{a}_i$	Band 4	Band 5	Band 6	Band 7	% Var. Accounted For	Std. Dev. σ_i
ICE	19 JAN 76	i = 1	.46805	.64056	.59692	.11956	99.2	17.30
		2	-.58351	-.27129	.67717	.35688	0.6	2.02
		3	.65672	-.71177	.22932	.09757	0.1	0.82
		4	--	--	--	--	--	--
SEDIMENT	24 FEB 76 (North)	i = 1	.51714	.71712	.46722	.00397	96.5	4.22
		2	-.52185	-.16851	.83612	.01373	2.5	0.99
		3	.67830	-.67623	.28724	-.01093	0.9	0.61
		4	--	--	--	--	--	--
	24 FEB 76 (South)	1	.48809	.73104	.47652	.01645	95.3	3.71
		2	-.52581	-.17978	.82233	.06607	3.6	1.09
		3	.68866	-.65819	.30404	.00964	1.1	0.60
		4	.02078	.00621	-.06526	.99763	0.1	0.20
	19 JAN 76	1	.51756	.76911	.37497	0	95.3	2.69
		2	-.16507	-.34025	.92573	0	3.4	0.84
		3	.83957	-.54102	-.04914	0	1.2	0.49
		4	--	--	--	--	--	--
	AVERAGE	1	.50760	.73910	.43957	.00681		
		2	-.40758	-.22951	.86139	.02660		
		3	.73551	-.62515	.18071	.00043		
		4	--	--	--	--		
CLOUDS	19 JAN 76	i = 1	.42651	.59482	.62637	.26821	99.8	29.1
		2	.66526	.30245	-.60425	-.31745	0.1	1.09
		3	--	--	--	--	--	--
		4	--	--	--	--	--	--
	19 AUG 75	1	.65527	.53892	.49356	.18967	96.3	4.31
		2	-.59143	.72833	-.13235	.31973	1.8	0.68
		3	-.46911	-.15480	.85434	-.16147	1.2	0.55
		4	-.01206	-.39389	.09479	.91418	0.8	0.43

Date	Eigen-vector $\hat{a}_i$	Band 4	Band 5	Band 6	Band 7	% Var. Accounted For	Std. Dev. σ_i
15 MAR 74	i = 1	.52965	.60448	.56532	.18527	85.7	1.99
	2	-.84545	.34518	.36073	.18956	6.8	0.69
	3	.01586	.47497	-.69849	.53503	4.9	0.59
	4	.06660	-.53838	.24979	.80207	2.6	0.42
AVERAGE	1	.53714	.57941	.56175	.21453		
	2						
	3	No apparent directional preference					
	4						

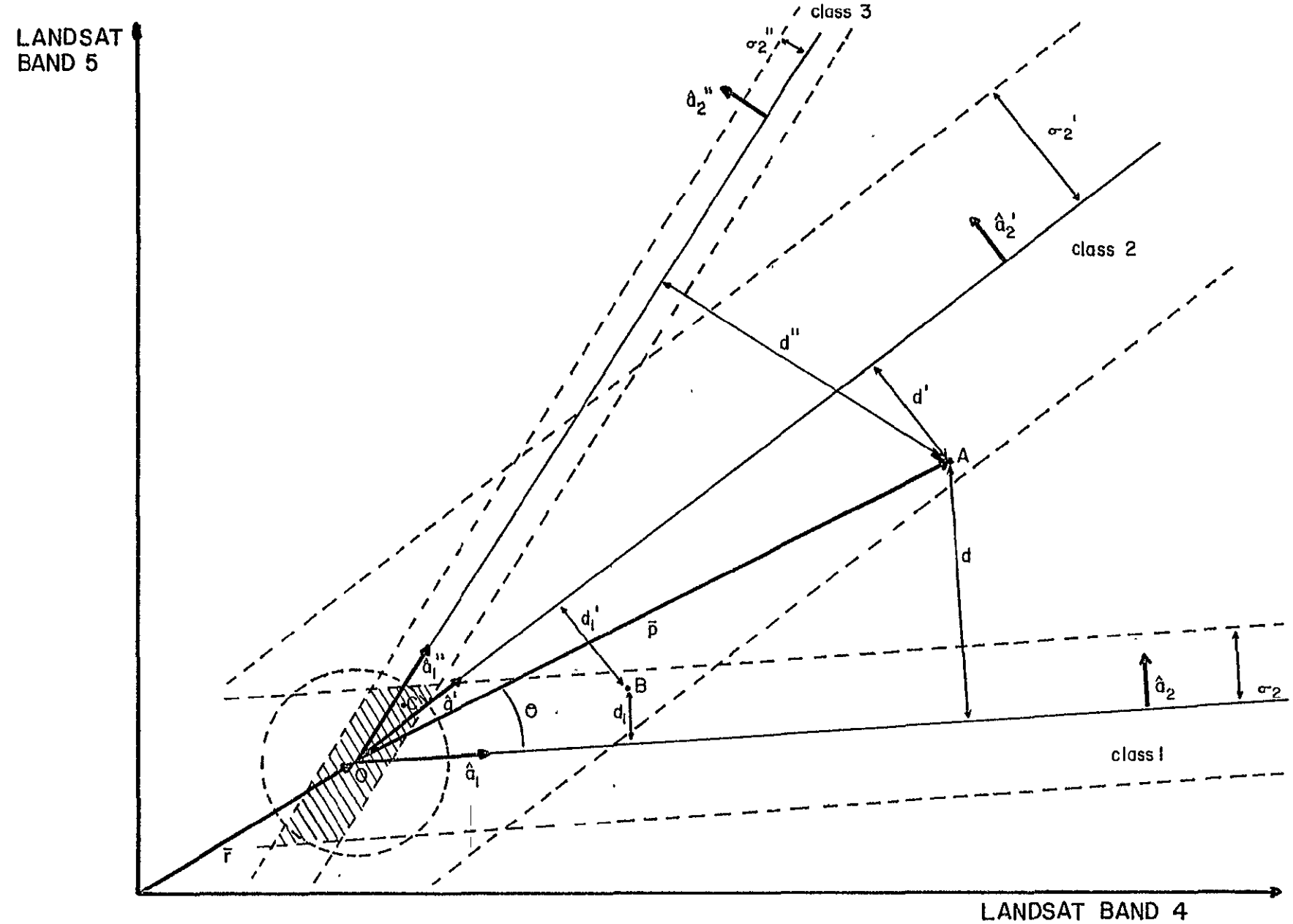

Figure 3.13. The eigenvector geometry applied to spectral classification.

have chosen a distance of two standard deviations. The "clear" water mean is represented by o and $\vec{r}$ is the vector distance from the original color space origin to the clear water mean. A point at position A clearly belongs to class 2 since it is within two standard deviations of axis of this class ($d' < 2\sigma_2'$) and well outside the same range of the other two classes ($d > 2\sigma_2$, $d'' > 2\sigma_2''$). The first step then is to find the distance of the test point axis of each of the classes and throwing out any class that is too far away. The distance d is given by:

$$d = |\overline{p} \times \hat{a}_1| = p \; a \; \sin\theta \tag{3.21}$$

A point at position B (Figure 3.13) is more difficult to assess since it is sufficiently close to the axes of both class 1 and class 2. The simplest criterion in this case is if the distance to one class relative to the two standard deviation limit of that class is less than the distance to the second class relative to the two standard deviation limit in that class. That is, if

$$\frac{d_1'}{2\sigma_2'} < \frac{d_1}{2\sigma_2} \tag{3.22}$$

Then the point is classified as belonging to class 2. The same sort of process could be used to place point C in one class or another. However, point C is within range of all three classes (the area for which all three classes overlap is the shaded area in Figure 3.13) and it is not clear that the classification procedure is really sensitive enough to make meaningful distinction among the classes. For the present the above criterion (equation 3.22) will be used in this region. In the future, another

criterion may prove to be more valuable in this area.

Finally, we must set the limit on being able to distinguish a target spectrum from that of clear water. There are several choices the most obvious of which is to define a some ellipsoid centered on the origin 0 within which all the point are assumed to be representative of clear water. This is represented by the circle in Figure 3.13. The size of the circle was intentionally chosen to nearly cover the shaded areas, thus implying that any points falling within the classification ranges of more than two classes be most accurately classified as clear water. Certainly, this is likely to be a reasonable assumption in the present case where there are only four classes to be tested and only two of those actually in water. Since this is computationally a little more efficient this is the criterion we will use here.

There are several ways in which the classification accuracy can be improved (as it may have to be as more classes are added to the process). The distributions shown in Figure 3.13 are highly idealized. They may not be entirely realistic. A more sophisticated approach would be to use the training data to derive a statistical function to represent the distribution of data points within the class. Thus, for the example of point B, even if d_1 and d_1' were equal, the distribution functions of the two classes might differ, solving the classification problem.

It is also possible that the distribution patterns are not always radially outward from the clear water origin but have bends or twists. This sort of thing has not been seen in the present study, but it is not hard to imagine a situation in which the spectral reflectance characteristics of a substance in water are not linear with increasing

concentration. If such a distribution should be encountered a more elaborate classification scheme would be needed to properly treat the case.

For the present, the simpler classification scheme should suffice. Summarizing the procedure is as follows (refer to Figure 3.13):

1) Find the vector $\bar{p}$ for the test pixel. If the pixel is described by vector $\bar{b} = (b_1, b_2, b_3, b_4)$ where b_1 is the intensity (in counts) in Band 4, etc., and the "clear" water is given by $\bar{r} = (r_1, r_2, r_3, r_4)$, then $\bar{p}$ is given by

$$\bar{p} = \bar{b} - \bar{r} \tag{3.23}$$

2) Find the perpendicular distance d from the test pixel at point A to the axis of each classification distribution.

$$d = |\bar{p} \times \hat{a}_1| = p \; a \; \sin\theta \tag{3.24}$$

where $\hat{a}_1$ is the primary eigenvector for some class and θ is the angular separation of $\bar{p}$ and $\hat{a}_1$.

3) Test to see if this distance falls within the cutoff range ($d < 2\sigma_2$). This cutoff can be set as strictly or loosely as one might like. The scaling factor is the standard deviation σ_2 along the second eigenvector (Table 3.3).

4a) If A is within $2\sigma_2$ of only one class the classification is finished.

b) If A is within $2\sigma_2$ of two classes then it should be placed in that class for which the ratio of d/σ_2 is smallest.

c) If A is within $2\sigma_2$ of more than two classes then it is classified as water.

d) If A is not within $2\sigma_2$ of any class it is unclassified.

There is one further step that can be taken. It seems reasonable that the displacement of a point along one of the first eigenvectors should be related to some physical property of the water. Intuitively, the concentration of a substance in the water would be the most likely parameter, the argument being that the addition of a large amount of the material to the water would shift the spectral reflectance characteristics more than the addition of a small amount of the same material. The actual relationship could be quite complicated and we will not deal with that problem here. Still, we can certainly make a qualitative assessment of concentration.

The displacement of a point along the direction of the first eigenvector is given by

$$s = \bar{p} \cdot \hat{a}_1 = pa_1 \cos\theta \tag{3.25}$$

If we choose σ_1 (see Table 3.3) as our unit of length then we can define levels of "concentration", c, such that

$$\begin{aligned} c &= c_1 \text{ for } 0 < s/\sigma_1 < 1 \\ &= c_2 \text{ for } 1 \leq s/\sigma_1 < 2 \\ &= c_n \text{ for } (n-1) \leq s/\sigma_1 < n \quad . \end{aligned} \tag{3.26}$$

This is the procedure which will be used in this report.

3.3.2 Results and Discussion

To illustrate the use of this analysis let us consider the 19 January 1976 Landsat scene (Fig. 3.8). In this scene, although the acid waste dump is partially obscured by clouds, the plume can be distinguished by its distinctive shape. The approximate position of the training sets is shown in the insert of Fig. 3.8 and the coordinates of the clear water training set are given in Table 3.2. The training sets were chosen to be as large as possible, given the limitations imposed by a square training area, and were distributed over the plume to cover as large a range of concentrations as possible. Each training set was a multiple of 6 pixels along the scan lines in order to minimize any effects of the 6 line banding in the data. Only three eigenvectors were used for training in this area -- those for acid, clouds and sediment (Table 3.3). Ice was excluded in order to reduce processing time. The sediment training sets, which are not shown, were taken from the turbid areas off of Cape Henlopen, Delaware (Fig. 3.8).

For the first trial the classification limits were chosen to be three standard deviations for all three classes, i.e. $\sigma_2 = \sigma_2' = \sigma_2'' = 3$. Thus, any pixel which fell within three σ_2 of any of the class axes would be classified, and any pixel falling within $3\sigma_2$ of all three would be classified as water (3-class rule). At these classification limits, the system did not misclassify clouds or sediments as acid, but it did seem to be missing much of the acid. What happened is that most of the pixels that should have been classified as acid had position vectors $\bar{p}$ that were too close to the origin and were also falling within the class

limits of clouds and sediment and were thus being classified as water.

One way to improve the classification would be to define a separate standard for water, independent of the 3-class rule. This sort of thing is illustrated by the circle about the origin in Figure 3.13. Here, since our target is acid and we are relatively unconcerned with a loss in accuracy in identifying clouds or sediment, we can tighten the class limits for clouds and sediment by requiring that a pixel be within two standard deviations of the class axis for sediment and clouds, but need only be within three standard deviations of the class axis for acid. The results of applying this requirement are shown in Figure 3.14. This is quite an improvement. With these limits, far more of the acid is properly classified, largely at the expense of the cloud class. A little more than 8% of the pixels were unclassified and only 83 were classified as sediment. Twenty-five percent were classed as clouds and 64% were classed as water.

The next test is to try the classification method on a Landsat scene in which the acid plume is not as clearly identifiable by shape. The 15 March 1974 overpass suits this purpose nicely (Fig. 3.12). The figure 8 pattern is not evident and the acid is very similar in contrast to the clouds. Using the eigenvectors in Table 3.3 for this day, and setting $\sigma_2 = 3$, and $\sigma_2' = \sigma_2'' = 2$, the analysis was performed and the results are shown in Figure 3.15. The classification is still rather good but it is not without flaws. The cloudy area adjacent to the acid (lower right in Figure 3.15) is classified properly. This is the area in which cloud training sets were taken. Away from this region the

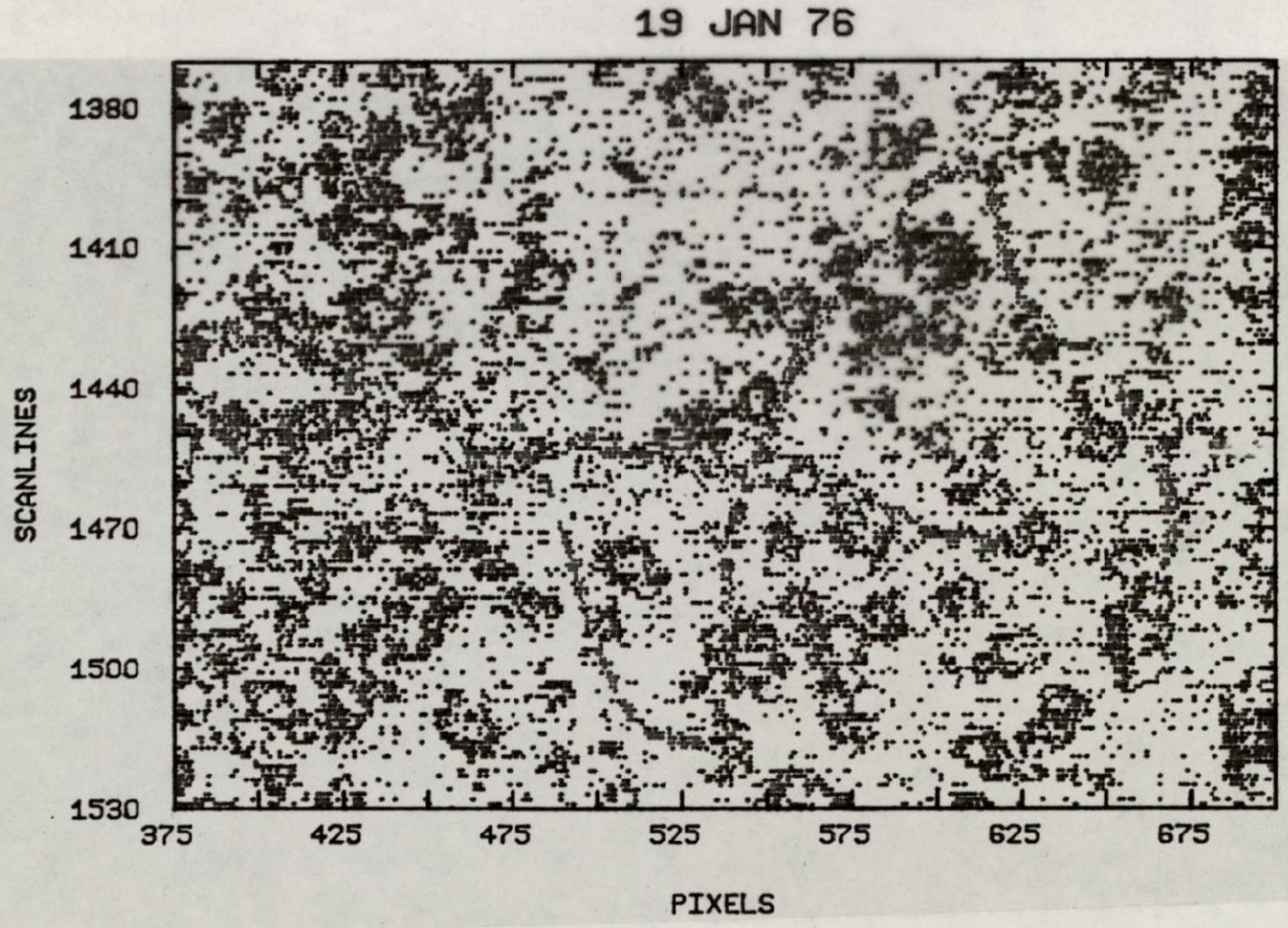

Figure 3.14. The iron-acid waste plume of 19 January 1976. The overlay shows the pixels classified as clouds.

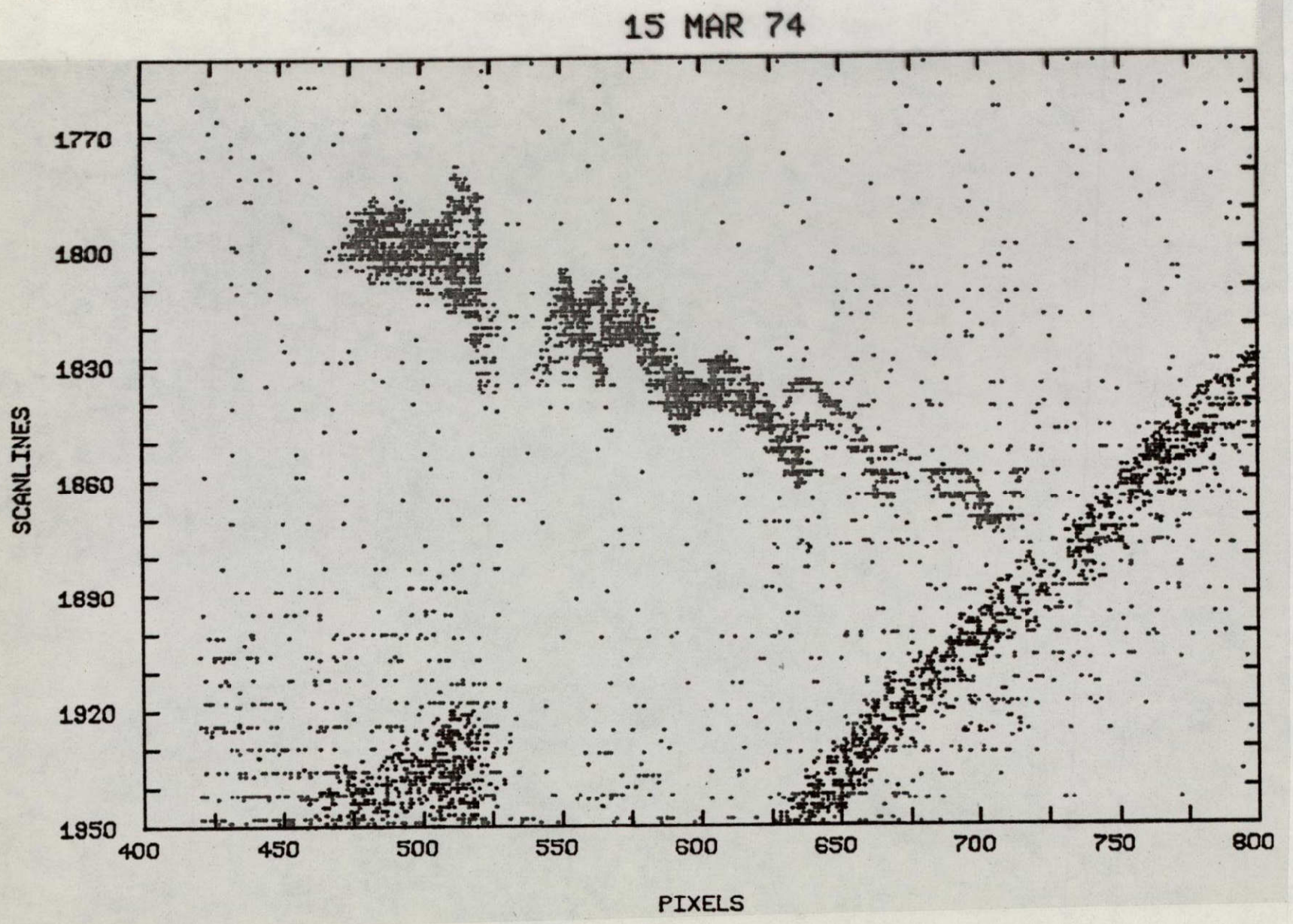

Figure 3.15. The iron-acid waste plume of 15 March 1974. The overlay shows the pixels that were classified as clouds.

classification deteriorates somewhat and begins to confuse clouds with acid. The number of unclassified pixels also increases.

As a final test of the validity of using the eigenvector analysis for classification of water types, the principal eigenvectors for acid, sediment, clouds and ice were computed for six different Landsat overpasses. The angular separation of these vectors was then calculated assuming a common "clear" water origin (see Table 3.2). The results are listed in Table 3.4. The angular separation among the eigenvectors for acid is ~10°, as is the separation among the cloud eigenvectors. The angular separation among the sediment eigenvectors is about 5°.

In contrast the angles between different target eigenvectors are significantly larger except for clouds and ice. In particular, note that the angles separating the vectors for acid and sediment (~30°) are only slightly less than those for acid and clouds (~35°). This implies that, had a sediment plume been in the area of the acid dump, the two could have been readily distinguished from one another. This is very promising as far as identifying a plume as being one substance or another. At this point it is uncertain what will happen when the two substances are mixed. This would be an area for further study.

			IRON-ACID WASTE							SEDIMENT				CLOUDS				ICE
			24 FEB 76	19 JAN 76	21 OCT 75	19 AUG 75	17 NOV 75	15 MAR 74	AVERAGE	24 FEB 76 (NORTH)	24 FEB 76 (SOUTH)	19 JAN 76	AVERAGE	19 JAN 76	19 AUG 76	15 MAR 74	AVERAGE	19 JAN 76
			1	2	3	4	5	6	7	8	9	10	11	12	13	14	15	16
ACID	24 FEB 76	1	--															
	19 JAN 76	2	14.4	--														
	21 OCT 75	3	3.9	13.7	--													
	19 AUG 75	4	12.7	6.2	10.5	--												
	17 NOV 75	5	4.4	13.6	7.8	13.8	--											
	15 MAR 74	6	6.3	10.7	8.6	11.6	3.3	--										
	AVERAGE	7	8.5	11.1	8.6	10.3	8.8	7.9	--									
SEDIMENT	24 FEB 76	8	36.1	22.9	33.9	23.7	36.4	33.5	31.5	--								
	24 FEB 76	9	37.9	24.8	35.7	25.4	38.3	35.4	33.3	2.0	--							
	19 JAN 76	10	34.2	22.6	31.4	21.8	35.2	32.7	30.1	6.1	6.5	--						
	AVERAGE	11	36.1	23.5	33.7	23.6	36.6	33.8	31.8	3.6	3.9	5.1	--					
CLOUDS	19 JAN 76	12	47.2	33.8	45.9	35.7	46.1	42.9	42.2	19.8	18.9	24.1	21.0	--				
	19 AUG 76	13	31.6	18.5	30.8	21.3	30.2	26.9	27.0	16.9	17.8	20.2	18.3	16.2	--			
	15 MAR 74	14	39.4	25.7	38.1	27.8	38.4	35.2	34.5	13.5	13.4	18.0	15.1	8.3	9.2	--		
	AVERAGE	15	39.8	26.7	38.7	28.8	38.7	35.5	35.0	16.9	16.9	20.9	18.3	10.5	10.8	7.2	--	
ICE	19 JAN 76	16	42.6	28.6	41.1	30.6	41.9	38.7	37.6	11.2	10.5	16.5	13.0	9.4	14.3	5.9	10.4	--
	AVERAGE																	

Table 3.4. Angular separation (in degrees) between primary eigenvectors.

3.4 Conclusions

Eigenvector analysis using a "clear" water origin has been applied to spectral data for the purpose of classifying substances in water. The preliminary trials described here show that the approach is valid and quite promising. These trials are really just a first attempt and can probably be improved upon.

There are several things that can be done to improve the classification. The first is to define the limits for "clear" water independently of the other targets (3-class rule). This should make it unnecessary to arbitrarily weigh the class limits in favor of the preferred target. (In an operational system, an optional weighting in favor of a preferred target could be useful.

The second improvement would come simply from expanding the data base. In Figure 3.16 misclassification seems to be due to the limited data base for clouds. Increasing the data base for the targets should improve the classification by adjusting the orientation of the eigenvectors and by improving the estimates of the σ_2's -- the scatter of the data. Increasing the size of the data base also raises the possibility of directly determining the probability distribution of the data about the class axis. In the present analysis the distributions are unspecified but are assumed to be symmetric about the class axis and the same for all classes. If the data base is large enough the probability distributions could be determined. These more realistic

distributions would then be used to derive weighting functions which would be used instead of the σ_2's in choosing the most likely of two or more classes.

The only major drawback to this approach is the necessity of defining a "clear" water base signature. For many important applications no "clear" water appears in the Landsat scene. Even in the examples presented here, there is no assurance that the "clear" water standards really refer to the ideal standard water mass. As is implied by the quotes, the clarity of the water is only relative. Even so, the procedure seems to work remarkably well and using the ideal standard provides a good conceptual and operational framework for the classification procedure.

Further research along these lines include a review of ways of estimating the ideal water standard without using training set data. If such an estimate can be made with sufficient accuracy it would enhance the value of this method tremendously.

REFERENCES

Apel, J. R., R. L. Charnell and R. J. Blackwell. 1974. Ocean internal waves off the North American and African coasts from ERTS-1. Proceedings of the Ninth International Symposium on Remote Sensing of Environment, Ann Arbor, Michigan, 15-19 April 1974.

Arvesen, J. C., J. P. Millard and E. C. Weaver. 1973. Remote sensing of chlorophyll and temperature in marine and fresh water. Astronautica Acta 18: 229-239.

Austin, R. W. 1974. The remote sensing of spectral radiance from below the ocean surface. In: Optical Aspects of Oceanography, Chapter 14, N. G. Jerlov and E. S. Nielsen, eds. Academic Press, New York.

Boileau, A. R. 1964. Atmospheric properties. Applied Optics 3: 570-581.

Duntley, S. Q. 1974. Underwater visibility and photography. In: Optical Aspects of Oceanography, Chapter 7, N. G. Jerlov and E. S. Nielsen, eds. Academic Press, New York.

Gordon, H. R., O. B. Brown and Jacobs. 1975. Computed relationships between the inherent and apparent optical properties of a flat homogeneous ocean. Applied Optics 14: 417-427.

Gordon, J. I. 1969. Directional radiance (luminance) of the sea surface. SIO Reference 69-20, Scripps Institute of Oceanography, Univ. of California, San Diego.

Gershun, A. 1939. The light field. J. Mathematical Physics 18: 51-151.

Hogan, R. P. 1974. A comparison between turbidity and seston concentration in Delaware Bay. Unpublished report, College of Marine Studies, University of Delaware.

Hulbert, E. O. 1943. Propagation of light in a scattering and absorbing medium. J. Optical Society America 33: 42-45.

Jain, S. C. and J. R. Miller. 1976. Subsurface water parameters: Optimization approach to their determination from remotely sensed water color data. Applied Optics 15: 886-890.

Johnson, R. W. 1975. Quantitative sediment mapping from remotely sensed multispectral data. Proceedings of the Fourth Conference on Remote Sensing of Earth Resources, Tullahoma, Tenn., March 24-26.

Johnson, R. W., C. W. Ohlhorst and J. W. Usry. 1977. Location, identification and mapping of sewage sludge and acid waste plumes in the Atlantic coastal zones.

Kagan, V. K. and Kondrat'ev, K. Y. 1971. Elements of the information theory of atmospheric visibility. Israel Program for Scientific Translation, Jerusalem.

Kattawar, G. W. and G. N. Plass. 1972. Radiative transfer in the earth's atmosphere-ocean system: II. Radiance in the atmosphere and ocean. J. Physical Oceanography 2: 146-156.

Kattawar, G. W., G. N. Plass and J. A. Guinn, Jr. 1973. Monte Carlo calculations of the polarization of radiation in the earth's atmosphere-ocean system. J. Physical Oceanography 3: 353-372.

Klemas, V., M. Otley, W. Philpot and R. Rogers. 1974. Correlation of coastal water turbidity and circulation with ERTS-1 and Skylab imagery. Proceedings of the Ninth International Symposium on Remote Sensing of Environment, Ann Arbor, Mich.

Klemas, V. and W. Philpot. 1976. Spectral reflectance signatures of coastal pollutants. Progress report, Contract NSG 1149, NASA Langley Research Center, Hampton, Va., Oct. 18, 1976.

Klemas, V. and W. Philpot. 1977. Determination of spectral reflectance signatures of coastal pollutants. Progress report, Contract NSG 1149, NASA Langley Research Center, Hampton, Va., June 3, 1977.

Klemas, V. and D. F. Polis. 1977. Remote sensing of estuarine fronts and their effects on pollutants. Photogrammetric Eng. and Remote Sensing 43(5): 599-612.

Lewis, B. W. and V. G. Collins. 1977. Remotely sensed and laboratory spectral signatures of an ocean-dumped acid waste. NASA TN D-8467, NASA Langley Research Center, Hampton, Va.

Maul, G. A., R. L. Charnell and R. H. Qualset. 1974. Computer enhancement of ERTS-1 images for ocean radiances. Remote Sensing of Environment 3: 237-253.

Maul, G. A. and H. R. Gordon. 1975. On the use of the Earth Resources Technology Satellite (Landsat-1) in optical oceanography. Remote Sensing of Environment 4: 95-128.

McCluney, W. R. 1974. Ocean color spectrum calculations. Applied Optics 13: 2422-2429.

Morrison, D. F. 1976. Multivariate Statistical Methods. McGraw-Hill, New York. 2nd edition.

Mueller, J. L. 1976. Ocean color spectra measured off the Oregon coast: characteristic vectors. Applied Optics 15: 394-402.

Nicodemus, F. E. 1963. Radiance. American J. Physics 31: 368-377.

Simmonds, J. L. 1963. Application of characteristic vector analysis to photographic and optical response data. J. Optical Society America 55: 968-974.

Stamm, G. L. and R. A. Langel. 1961. Some spectral irradiance measurements of upwelling light off the east coast of the United States. J. Optical Society America 51: 1090-1094.

Tabor, P. S. 1975. Evaluation of chlorophyll measurements by differential radiometry from aircraft altitudes. Master's thesis, College of Marine Studies, Univ. Delaware, Newark, Delaware.

Taylor, A. H. and G. P. Kerr. 1941. The distribution of energy in the visible spectrum of daylight. J. Optical Society America 31: 3-8.

Zaneveld, J. R. V. 1974. New developments of the theory of radiative transfer in the oceans. In: Optical Aspects of Oceanography, Chapter 6, N. G. Jerlov and S. Nielsen, eds. Academic Press, New York.

Zaneveld, J. R. V. and H. Pak. 1972. Some aspects of the axially symmetric submarine daylight field. J. Geophysical Research 77: 1689-1694.

APPENDIX A - INSTRUMENTATION

A.1 Transmissometer

The transmissometer used in the experiments described here was a Hydroproducts beam transmissometer model 612S. The path length used was 10cm. The spectral response of the instrument is very nearly photometric, i.e. close to the spectral response of the human eye. Maximum sensitivity of the instrument is at ~550nm.

The optical system is enclosed in a tube to exclude external light sources. The tube is open at either end to allow free flow of water through the optical system. Also, the tube has a flat black coating on the inner surface to absorb the light scattered from the beam.

A.2 Spectroradiometer

The spectroradiometer was a United Detector Technology (UDT) Model 1100B. This is a continuous scanning device which is sensitive to the range of wavelengths from .4μ to 1.1μ. The spectral separation is accomplished using two circularly variable interference filters, one for the visible (400-700nm) and one for the infrared (700-1100nm). The bandwidth of the visible range filter is 17nm while the bandwidth of the infrared range filter is a little broader -- about 25nm. The data for the visible region is presented in 10nm increments. This is meant to facilitate comparison with other sensors and is not meant to imply any improvements in the spectral resolution.

The response of the 1100B is flat over the entire region of sensitivity. This is accomplished by using a variable aperture size. As the detector sensitivity decreases, the aperture size increases, thus increasing the area of the detector which is illuminated. This requires a diffusing plate in the input optics to insure that the illumination is uniform over the largest possible aperture area (figure A.1). Unfortunately this diffusion is not

Lambertian. In fact, the response is quite directional and departs significantly from cosine response (figure A.2). This places a constraint on using the 1100B with extended sources; the field of view must be limited to a small solid angle. For this reason the 1100B was fitted with a Gershun tube giving a field of view with a half angle of 4° or a solid angle of .0153 steradians.

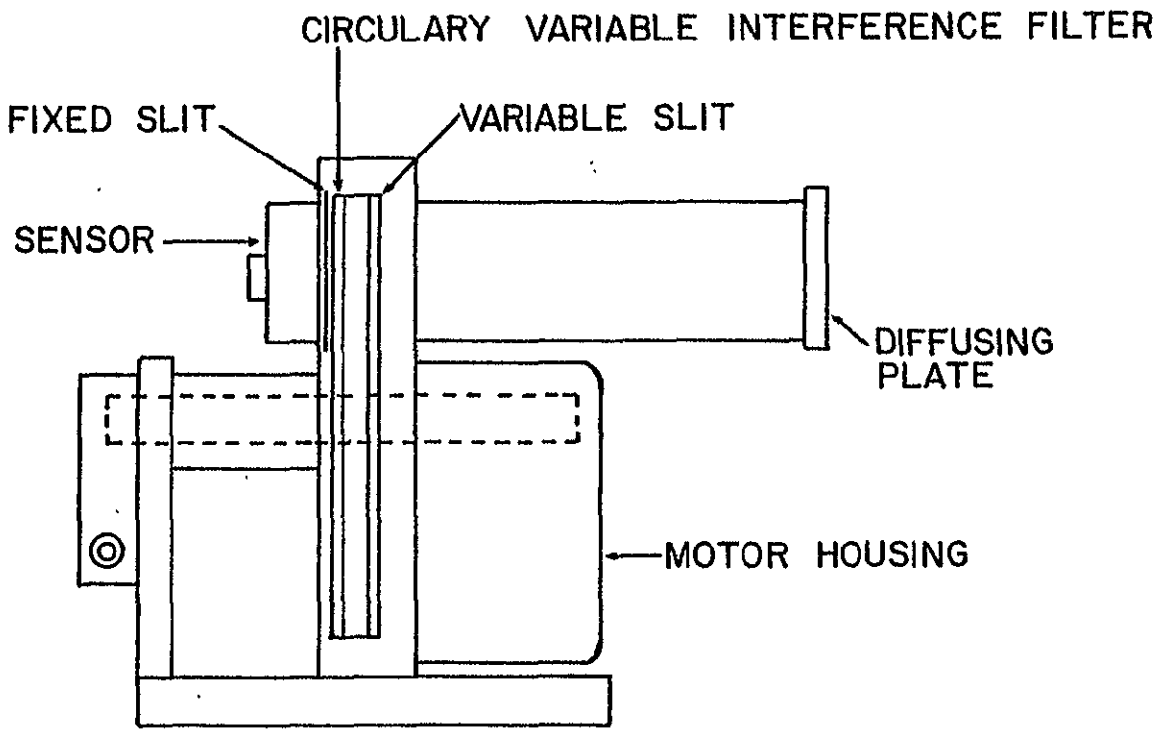

Figure A.1 - United Detector Technology (UDT) Spectroradiometer

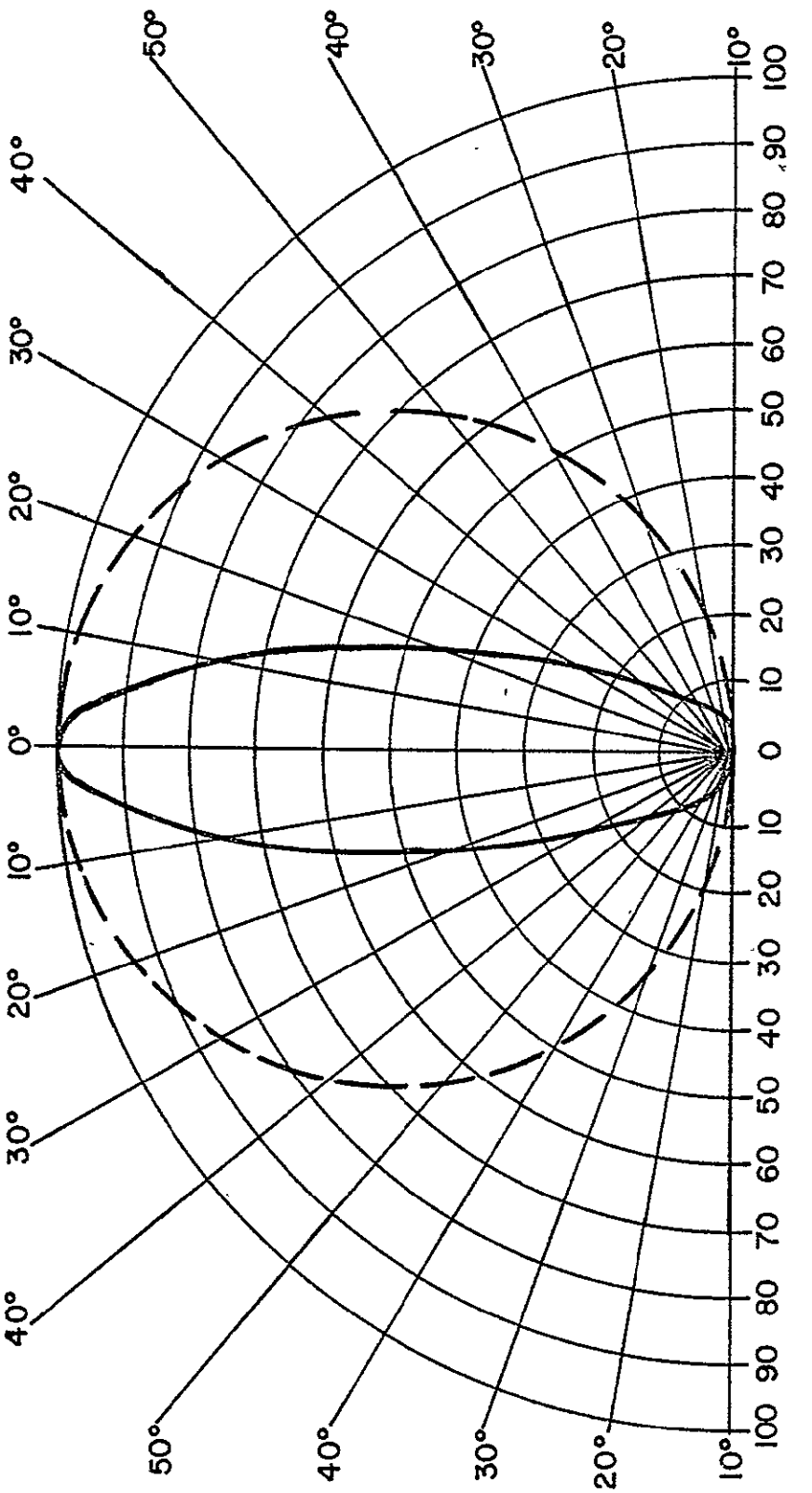

Figure A.2 - Directional Response of the Diffusing Plate.

APPENDIX B - DATA

WAVELENGTH (nm)	1100	1200	1300	1400	1500	1600	1700
405	62.5	63.5	66.7	57.3	48.1	38.1	26.0
415	72.1	73.5	76.8	68.4	56.6	45.8	31.5
425	78.6	79.9	81.1	74.5	64.4	51.3	36.2
435	86.9	93.8	95.4	85.4	71.0	58.7	42.0
445	103.0	106.0	106.0	97.6	82.0	69.9	51.2
455	113.0	116.0	118.0	109.0	91.0	80.0	58.8
465	116.0	121.0	121.0	114.0	98.2	85.9	63.6
475	120.0	125.0	127.0	117.0	102.0	90.9	68.0
485	122.0	125.0	127.0	118.0	103.0	93.1	68.0
495	122.0	125.0	126.0	118.0	104.0	93.5	69,4
505	123.0	125.0	127.0	119.0	194.0	96.7	71.6
515	123.0	125.0	127.0	120.0	104.0	97.1	72.6
525	124.0	125.0	127.0	121.0	106.0	100.5	75.2
535	122.0	123.0	124.0	117.0	106.0	98.5	75.5
545	118.0	122.0	120.0	115.0	104.0	95.3	72.2
555	116.0	120.0	119.0	114.0	103.0	95.2	72.5
565	115.0	119.0	118.0	113.0	103.0	95.4	72.5
575	114.0	117.0	118.0	112.0	102.0	94.7	71.9
585	114.0	116.0	117.0	111.0	102.0	94.9	72.1
595	114.0	116.0	119.0	114.0	103.0	97.6	74.4
605	115.0	117.0	120.0	114.0	104.0	101.1	77.4
615	116.0	117.0	121.0	115.0	106.0	103.0	79.5
625	115.0	114.0	118.0	113.0	105.0	101.4	79.3
635	112.0	114.0	117.0	110.0	104.0	98.4	76.7
645	109.0	109.0	110.0	105.0	98.5	94.8	74.4
655	105.0	106.0	108.0	104.0	97.0	92.9	73.1
665	105.0	106.0	108.0	105.0	97.0	95.9	75.6
675	106.0	107.0	110.0	107.0	97.8	98.0	78.2
685	106.0	107.0	110.0	107.0	97.8	98.2	77.9
695	105.0	106.0	110.0	107.0	97.8	96.8	77.4
712	107.9	114.0	112.0	110.0	102.2	101.1	81.0
737	102.7	104.0	104.0	99.6	94.2	89.6	71.1
762	85.8	86.0	87.0	86.0	79.7	79.6	62.8
787	91.3	89.0	90.0	89.0	85.9	85.8	69.7
812	81.6	81.0	82.0	79.1	74.9	76.2	57.5
837	75.9	76.0	76.0	74.9	69.7	68.8	55.6
862	72.9	73.0	73.0	71.7	68.3	68.4	56.4
878	69.2	68.0	70.0	67.3	65.4	65.6	53.2
912	53.5	55.0	59.0	54.1	51.7	47.6	36.4
937	35.7	37.0	37.0	33.7	31.7	27.5	17.9
962	32.6	35.0	35.0	32.0	27.9	25.5	19.8
987	46.5	45.0	48.0	47.5	42.6	45.3	37.7
1012	49.7	49.0	49.0	50.4	48.2	51.5	42.5
1037	47.0	48.0	49.0	49.1	47.0	48.7	40.1
1062	43.3	45.0	45.0	46.0	44.4	44.2	36.4
1087	34.3	36.0	35.0	35.3	32.8	36.4	27.2

Table B.1 - Solar Irradiance ($mw/cm^2/\mu$)

WAVELENGTH (nm)	1100	1200	1300	1400	1500	1600	1700
405	10.10	12.40	12.00	11.00	9.87	7.71	4.71
415	10.80	13.20	13.20	11.70	10.40	8.09	5.06
425	11.10	13.40	13.40	11.80	10.60	8.15	5.09
435	11.30	14.00	13.80	12.10	10.90	8.41	5.15
445	12.10	15.30	15.00	12.70	11.50	8.90	5.50
455	12.60	15.90	15.70	13.20	11.80	9.06	5.66
465	12.60	15.90	16.00	13.00	11.60	9.00	5.56
475	12.60	15.70	15.80	12.60	11.20	8.99	5.31
485	11.70	14.70	14.50	11.90	10.40	8.01	4.90
495	11.30	14.30	14.20	11.20	10.00	7.62	4.59
505	10.90	13.70	13.50	10.80	9.44	7.20	4.35
515	10.40	13.30	13.30	10.30	8.99	6.84	4.10
525	10.10	13.10	12.40	9.97	8.64	6.56	3.90
535	9.28	11.90	11.70	9.12	7.74	5.93	3.51
545	8.76	11.40	11.20	8.49	7.27	5.44	3.22
555	8.40	11.00	11.20	8.11	6.86	5.20	2.99
565	7.97	10.50	11.20	7.68	6.44	4.78	2.75
575	7.68	10.20	10.40	7.26	6.16	4.58	2.61
585	7.45	9.71	10.10	6.99	5.90	4.27	2.44
595	7.42	9.71	10.00	6.87	5.85	4.21	2.42
605	7.42	9.71	10.00	6.84	5.78	4.14	2.36
615	7.42	9.71	10.00	6.79	5.69	4.06	2.30
625	7.09	9.29	9.70	6.41	5.26	3.82	2.14
635	6.70	9.02	9.20	6.09	4.98	3.57	2.02
645	6.34	8.52	8.70	5.64	4.66	3.33	1.83
655	6.11	8.30	8.40	5.46	4.54	3.20	1.81
665	6.11	8.30	8.40	5.45	4.54	3.18	1.80
675	6.11	8.30	8.40	5.45	4.53	3.18	1.80
685	6.11	8.33	8.40	5.45	4.53	3.14	1.78
695	6.11	8.33	8.40	5.45	4.46	3.06	1.76
712	5.49	7.91	7.92	4.99	3.77	2.35	1.42
737	5.03	7.14	7.05	4.29	3.30	2.02	1.18
762	4.12	4.14	5.80	3.55	2.71	1.60	0.95
787	4.12	5.92	5.99	3.53	2.60	1.54	0.96
812	3.76	5.28	5.36	3.13	2.27	1.33	0.76
837	3.76	4.83	4.88	2.80	2.04	1.10	0.66
862	3.27	4.65	4.68	2.66	1.90	1.04	0.52
887	3.07	4.26	4.38	2.48	1.76	0.95	0.54
912	2.42	3.48	3.41	1.90	1.32	0.68	0.38
937	1.67	2.30	2.37	1.25	0.88	0.44	0.20
962	1.47	2.01	2.00	1.08	0.61	0.31	0.19
987	1.60	2.75	2.64	1.26	0.82	0.36	0.26
1012	1.80	2.92	2.84	1.51	0.92	0.40	0.31
1037	1.83	2.85	2.77	1.47	0.95	0.40	0.29
1062	1.67	2.56	2.69	1.38	0.93	0.40	0.26
1087	1.44	2.00	2.14	1.17	0.77	0.33	0.20

Table B.2 - Zenith Sky Radiance ($mw/cm^2/\mu/steradian$)

WAVELENGTH (nm)	1100	1200	1300	1400	1500	1600	1700	MEAN	VARIANCE	PERCENT VARIATION
405	0.490	0.509	0.503	0.453	0.387	0.305	0.122	0.396	0.01996	0.35712
415	0.578	0.582	0.582	0.521	0.458	0.364	0.146	0.462	0.02587	0.34846
425	0.644	0.653	0.642	0.575	0.498	0.407	0.173	0.513	0.03072	0.34155
435	0.735	0.771	0.750	0.667	0.574	0.461	0.198	0.594	0.04263	0.34776
445	0.882	0.908	0.886	0.801	0.675	0.526	0.238	0.702	0.06092	0.35144
455	1.010	1.050	1.020	0.913	0.774	0.637	0.275	0.811	0.07829	0.34489
465	1.090	1.140	1.090	0.980	0.847	0.681	0.306	0.876	0.08931	0.34104
475	1.170	1.200	1.170	1.060	0.902	0.725	0.326	0.936	0.10206	0.34126
485	1.190	1.240	1.200	1.090	0.923	0.751	0.336	0.961	0.10670	0.33976
495	1.220	1.250	1.240	1.110	0.937	0.762	0.341	0.980	0.11212	0.34167
505	1.250	1.270	1.260	1.150	0.979	0.800	0.351	1.009	0.11443	0.33541
515	1.260	1.290	1.290	1.190	0.993	0.818	0.363	1.029	0.11748	0.33305
525	1.320	1.330	1.330	1.240	1.040	0.847	0.378	1.069	0.12601	0.33198
535	1.320	1.310	1.320	1.230	1.040	0.843	0.382	1.064	0.12228	0.32879
545	1.280	1.270	1.310	1.190	1.040	0.833	0.382	1.044	0.11360	0.32298
555	1.260	1.270	1.310	1.190	1.040	0.831	0.380	1.040	0.11266	0.32270
565	1.260	1.250	1.300	1.190	1.030	0.829	0.374	1.033	0.11174	0.32351
575	1.250	1.240	1.300	1.190	1.020	0.823	0.363	1.027	0.11312	0.32764
585	1.250	1.240	1.260	1.150	1.000	0.813	0.353	1.009	0.11053	0.32935
595	1.240	1.240	1.250	1.150	0.984	0.802	0.348	1.002	0.11079	0.33219
605	1.230	1.240	1.250	1.160	0.984	0.805	0.350	1.003	0.10989	0.33060
615	1.230	1.240	1.250	1.150	0.984	0.801	0.350	1.001	0.10964	0.33089
625	1.190	1.170	1.190	1.110	0.961	0.789	0.350	0.966	0.09559	0.32015
635	1.120	1.140	1.140	1.060	0.918	0.744	0.335	0.922	0.08826	0.32207
645	1.060	1.070	1.070	0.987	0.864	0.733	0.322	0.872	0.07481	0.31356
655	1.040	1.050	1.040	0.951	0.821	0.669	0.311	0.840	0.07431	0.32441
665	1.040	1.000	1.020	0.930	0.803	0.665	0.307	0.824	0.07005	0.32137
675	1.030	1.010	1.010	0.926	0.797	0.666	0.307	0.821	0.06916	0.32037
685	1.030	1.000	1.010	0.923	0.799	0.666	0.305	0.819	0.06876	0.32018
695	1.030	1.010	1.000	0.910	0.799	0.642	0.298	0.813	0.07082	0.32745
712	0.931	0.928	0.998	0.815	0.752	0.680	0.313	0.774	0.05368	0.29939
737	0.595	0.595	0.592	0.490	0.473	0.417	0.200	0.482	0.02025	0.29630
762	0.418	0.431	0.408	0.356	0.339	0.283	0.146	0.340	0.01002	0.29431
787	0.415	0.418	0.413	0.369	0.327	0.301	0.144	0.341	0.00966	0.28827
812	0.405	0.399	0.402	0.348	0.322	0.283	0.136	0.328	0.00929	0.29407
837	0.304	0.301	0.302	0.255	0.243	0.208	0.102	0.245	0.00530	0.29709
862	0.265	0.235	0.237	0.199	0.192	0.160	0.076	0.195	0.00395	0.32237
887	0.209	0.209	0.194	0.149	0.161	0.118	0.065	0.158	0.00281	0.33558
912	0.147	0.124	0.136	0.101	0.103	0.077	0.040	0.104	0.00135	0.35347
937	0.085	0.059	0.070	0.056	0.056	0.036	0.018	0.054	0.00048	0.40284
962	0.056	0.026	0.056	0.028	0.024	0.023	0.003	0.031	0.00036	0.61785
987	0.049	0.033	0.041	0.026	0.018	0.026	0.004	0.028	0.00022	0.52681
1012	0.049	0.046	0.044	0.028	0.018	0.024	0.005	0.031	0.00027	0.53744
1037	0.052	0.039	0.046	0.028	0.020	0.024	0.005	0.031	0.00026	0.53143
1062	0.052	0.033	0.049	0.029	0.021	0.028	0.005	0.031	0.00026	0.51981
1087	0.052	0.020	0.051	0.023	0.024	0.022	0.004	0.028	0.00030	0.62236

Table B.3 - Upwelling Radiance from the Tank Water ($mw/cm^2/\mu/steradian$)

C-2

WAVELENGTH (nm)	1100	1200	1300	1400	1500	1600	1700	MEAN	VARIANCE $\times 10^{-6}$	PERCENT VARIATION
405	0.00902	0.00785	0.00761	0.00797	0.00832	0.00942	0.00601	0.00803	1.2172	0.13738
415	0.00971	0.00820	0.00789	0.00823	0.00911	0.01041	0.00678	0.00862	1.4771	0.14101
425	0.01031	0.00899	0.00856	0.00880	0.00928	0.01121	0.00812	0.00932	1.1595	0.11549
435	0.01117	0.00962	0.00917	0.00953	0.01026	0.01187	0.00902	0.01009	1.1476	0.10618
445	0.01190	0.01029	0.00999	0.01057	0.01098	0.01213	0.00986	0.01081	0.8117	0.08330
455	0.01278	0.01127	0.01072	0.01120	0.01198	0.01383	0.01077	0.01179	1.3326	0.09788
465	0.01366	0.01204	0.01128	0.01186	0.01276	0.01432	0.01189	0.01254	1.2032	0.08744
475	0.01443	0.01256	0.01190	0.01289	0.01357	0.01483	0.01268	0.01327	1.1210	0.07981
485	0.01494	0.01431	0.01271	0.01352	0.01428	0.01598	0.01374	0.01408	1.1931	0.07757
495	0.01554	0.01369	0.01329	0.01410	0.01465	0.01652	0.01428	0.01458	1.2475	0.07659
505	0.01605	0.01417	0.01380	0.01475	0.01571	0.01739	0.01485	0.01525	1.5205	0.08088
515	0.01644	0.01458	0.01424	0.01546	0.01624	0.01809	0.01570	0.01582	1.6506	0.08121
525	0.01733	0.01516	0.01509	0.01622	0.01706	0.01857	0.01637	0.01654	1.5279	0.07472
535	0.01800	0.01561	0.01554	0.01694	0.01767	0.01937	0.01722	0.01719	1.8141	0.07834
545	0.01817	0.01542	0.01602	0.01693	0.01826	0.02011	0.01834	0.01761	2.5555	0.09079
555	0.01832	0.01579	0.01612	0.01726	0.01870	0.02034	0.01866	0.01789	2.5609	0.08947
565	0.01871	0.01586	0.01609	0.01763	0.01884	0.02073	0.01885	0.01810	2.9415	0.09474
575	0.01887	0.01608	0.01648	0.01801	0.01901	0.02092	0.01869	0.01829	2.6950	0.08974
585	0.01902	0.01643	0.01619	0.01767	0.01883	0.02099	0.01848	0.01823	2.7209	0.09049
595	0.01888	0.01643	0.01590	0.01738	0.01841	0.02031	0.01782	0.01788	2.2441	0.08380
605	0.01859	0.01633	0.01580	0.01755	0.01833	0.01990	0.01752	0.01772	1.9328	0.07847
615	0.01847	0.01633	0.01570	0.01730	0.01812	0.01959	0.01727	0.01754	1.7330	0.07505
625	0.01817	0.01587	0.01533	0.01714	0.01815	0.01980	0.01763	0.01744	2.2729	0.08644
635	0.01767	0.01557	0.01498	0.01690	0.01766	0.01938	0.01754	0.01710	2.1485	0.08572
645	0.01728	0.01532	0.01493	0.01658	0.01759	0.01995	0.01766	0.01705	2.8079	0.09831
655	0.01761	0.01546	0.01484	0.01620	0.01699	0.01863	0.01732	0.01672	1.7119	0.07824
665	0.01761	0.01468	0.01454	0.01571	0.01661	0.01806	0.01666	0.01627	1.8517	0.08366
675	0.01731	0.01472	0.01418	0.01540	0.01638	0.01776	0.01621	0.01599	1.7201	0.08201
685	0.01731	0.01456	0.01418	0.01535	0.01642	0.01778	0.01619	0.01597	1.8121	0.08430
695	0.01744	0.01482	0.01403	0.01512	0.01648	0.01741	0.01592	0.01589	1.7071	0.08223
712	0.01574	0.01299	0.01404	0.01342	0.01542	0.01857	0.01682	0.01529	3.9471	0.12996
737	0.01043	0.00886	0.00704	0.00879	0.01046	0.01282	0.01224	0.01033	2.8365	0.16302
762	0.00868	0.00847	0.00704	0.00735	0.00882	0.00987	0.01020	0.00863	1.3716	0.13566
787	0.00818	0.00716	0.00687	0.00743	0.00801	0.00990	0.00915	0.00810	1.1994	0.13521
812	0.00896	0.00761	0.00746	0.00793	0.00912	0.01054	0.01063	0.00889	1.7320	0.14801
837	0.00693	0.00596	0.00588	0.00607	0.00734	0.00861	0.00828	0.00701	1.2576	0.16000
862	0.00639	0.00464	0.00461	0.00483	0.00586	0.00662	0.00620	0.00559	0.7669	0.15659
887	0.00518	0.00441	0.00382	0.00371	0.00510	0.00504	0.00550	0.00468	0.4962	0.15053
912	0.00461	0.00292	0.00312	0.00307	0.00407	0.00450	0.00488	0.00388	0.6823	0.21287
937	0.00383	0.00176	0.00222	0.00260	0.00346	0.00349	0.00435	0.00310	0.8624	0.29946
962	0.00255	0.00031	0.00186	0.00110	0.00153	0.00242	0.00028	0.00144	0.8550	0.64392
987	0.00148	0.00022	0.00056	0.00059	0.00056	0.00157	0.00017	0.00073	0.3202	0.77013
1012	0.00130	0.00063	0.00058	0.00053	0.00044	0.00123	0.00023	0.00070	0.1619	0.57115
1037	0.00148	0.00040	0.00068	0.00056	0.00054	0.00130	0.00026	0.00074	0.2127	0.61935
1062	0.00168	0.00030	0.00093	0.00068	0.00063	0.00171	0.00034	0.00090	0.3415	0.65220
1087	0.00223	0.00000	0.00152	0.00065	0.00118	0.00161	0.00038	0.00108	0.6084	0.72059

Table B.4 - Volume Reflectance of the Tank Water

WAVELENGTH (nm)	1100	1200	1300	1400	1500	1600	1700	MEAN	VARIANCE	PERCENT VARIATION
405	0.357	0.511	0.590	0.546	0.410	0.382	0.101	0.427	0.01845	0.31831
415	0.451	0.622	0.698	0.659	0.495	0.454	0.226	0.515	0.02624	0.31451
425	0.523	0.766	0.776	0.765	0.534	0.503	0.256	0.589	0.03716	0.32727
435	0.641	0.859	0.944	0.905	0.680	0.596	0.293	0.703	0.05119	0.32204
445	0.793	0.115	0.121	0.109	0.842	0.722	0.372	0.883	0.08631	0.33283
455	0.978	1.310	1.440	1.340	0.999	0.851	0.436	1.051	0.12136	0.33160
465	1.120	1.460	1.580	1.510	1.130	0.948	0.479	1.175	0.14974	0.32926
475	1.260	1.630	1.750	1.670	1.260	1.030	0.534	1.305	0.18517	0.32977
485	1.380	1.710	1.910	1.730	1.360	1.110	0.565	1.395	0.20804	0.32696
495	1.460	1.860	2.060	1.910	1.450	1.180	0.609	1.504	0.25193	0.33369
505	1.580	1.960	2.170	2.030	1.560	1.260	0.656	1.602	0.27468	0.32710
515	1.700	2.110	2.350	2.110	1.710	1.360	0.700	1.720	0.31193	0.32472
525	1.860	2.320	2.480	2.320	1.860	1.480	0.759	1.868	0.39061	0.32140
535	1.920	2.370	2.520	2.370	1.890	1.500	0.773	1.906	0.37609	0.32173
545	1.910	2.370	2.560	2.410	1.910	1.510	0.774	1.921	0.38896	0.32473
555	2.000	2.520	2.680	2.470	1.990	1.590	0.799	2.007	0.42732	0.32571
565	2.070	2.580	2.740	2.520	2.040	1.620	0.810	2.055	0.44765	0.32556
575	2.080	2.570	2.730	2.520	2.050	1.630	0.813	2.056	0.44348	0.32388
585	2.090	2.580	2.710	2.470	2.020	1.590	0.802	2.037	0.44390	0.32701
595	2.090	2.560	2.670	2.410	1.980	1.560	0.795	2.009	0.43069	0.32662
605	2.080	2.510	2.530	2.350	1.890	1.510	0.778	1.950	0.39961	0.32423
615	2.050	2.460	2.480	2.270	1.830	1.460	0.750	1.901	0.38496	0.32633
625	1.900	2.300	2.360	2.150	1.710	1.380	0.720	1.789	0.34101	0.32650
635	1.840	2.170	2.220	2.060	1.560	1.290	0.675	1.688	0.31297	0.33145
645	1.710	2.030	2.060	1.890	1.500	1.200	0.639	1.576	0.26367	0.32591
655	1.610	1.880	1.930	1.750	1.390	1.110	0.595	1.466	0.22987	0.32695
665	1.520	1.820	1.840	1.650	1.320	1.040	0.565	1.394	0.21331	0.33142
675	1.480	1.750	1.790	1.620	1.270	1.010	0.554	1.353	0.19982	0.33028
685	1.490	1.720	1.790	1.630	1.260	1.010	0.554	1.351	0.19764	0.32917
695	1.470	1.680	1.780	1.590	1.240	1.000	0.550	1.330	0.18960	0.32739
712	1.380	1.530	1.720	1.470	1.050	0.905	0.499	1.222	0.18036	0.34753
737	0.670	0.651	0.766	0.694	0.484	0.408	0.235	0.558	0.03588	0.33927
762	0.390	0.438	0.513	0.450	0.297	0.266	0.143	0.357	0.01639	0.35884
787	0.390	0.477	0.524	0.443	0.284	0.252	0.143	0.359	0.01882	0.38209
812	0.390	0.449	0.493	0.422	0.265	0.246	0.139	0.344	0.01652	0.37406
837	0.270	0.306	0.364	0.325	0.206	0.180	0.100	0.250	0.00858	0.37035
862	0.190	0.293	0.297	0.246	0.144	0.144	0.073	0.198	0.00710	0.42551
887	0.170	0.224	0.270	0.216	0.114	0.121	0.065	0.169	0.00526	0.43037
912	0.120	0.173	0.183	0.154	0.072	0.083	0.041	0.118	0.00297	0.46184
937	0.065	0.119	0.119	0.082	0.042	0.046	0.022	0.071	0.00144	0.53636
962	0.046	0.086	0.069	0.052	0.016	0.036	0.013	0.045	0.00071	0.57597
987	0.042	0.082	0.069	0.081	0.013	0.031	0.018	0.048	0.00086	0.60953
1012	0.040	0.084	0.096	0.090	0.013	0.031	0.020	0.053	0.00125	0.66260
1037	0.040	0.082	0.088	0.086	0.013	0.033	0.018	0.051	0.00109	0.64155
1062	0.040	0.103	0.106	0.090	0.016	0.033	0.019	0.058	0.00160	0.68749
1087	0.040	0.079	0.098	0.064	0.023	0.029	0.020	0.050	0.00092	0.60091

Table B.5 - Upwelling Radinace from the Dockside Water ($mw/cm^2/\mu/steradian$)

WAVELENGTH (nm)	1100	1200	1300	1400	1500	1600	1700	MEAN	VARIANCE $\times 10^{-6}$	PERCENT VARIATION
405	0.00363	0.00539	0.00696	0.00758	0.00616	0.00942	0.00777	0.00670	3.4787	0.27836
415	0.00489	0.00654	0.00762	0.00866	0.00741	0.01074	0.00887	0.00782	3.4583	0.23790
425	0.00586	0.00863	0.00855	0.01016	0.00765	0.01171	0.01026	0.00897	3.7108	0.21465
435	0.00750	0.00883	0.01000	0.01153	0.01020	0.01344	0.01169	0.01045	3.8770	0.18833
445	0.00866	0.01148	0.01230	0.01306	0.01199	0.01504	0.01407	0.01237	4.2029	0.16572
455	0.01053	0.01252	0.01391	0.01534	0.01391	0.01688	0.01585	0.01414	4.6022	0.15177
465	0.01233	0.01398	0.01518	0.01730	0.01562	0.01850	0.01738	0.01575	4.6350	0.13665
475	0.01394	0.01577	0.01674	0.01937	0.01770	0.01971	0.01974	0.01757	4.9510	0.12666
485	0.01593	0.01727	0.01931	0.02055	0.01993	0.02241	0.02216	0.01965	5.7364	0.12188
495	0.01728	0.01929	0.02123	0.02348	0.02166	0.02447	0.02473	0.02173	7.6046	0.12688
505	0.01907	0.02086	0.02297	0.02527	0.02406	0.02630	0.02708	0.02366	8.4571	0.12292
515	0.02107	0.02293	0.02521	0.02661	0.02708	0.02903	0.02961	0.02593	9.6676	0.11990
525	0.02335	0.02559	0.02740	0.02954	0.02962	0.03143	0.03223	0.02845	10.1679	0.11207
535	0.02515	0.02744	0.02892	0.03180	0.03121	0.03341	0.03413	0.03029	10.6672	0.10782
545	0.02611	0.02801	0.03054	0.03344	0.03260	0.03526	0.03536	0.03633	14.1362	0.11835
555	0.02811	0.03060	0.03223	0.03494	0.03482	0.03777	0.03837	0.03383	14.0072	0.11063
565	0.02977	0.03201	0.03317	0.03639	0.03631	0.03930	0.04023	0.03531	14.7334	0.10870
575	0.03042	0.03257	0.03382	0.03715	0.03718	0.04019	0.04094	0.03604	15.3771	0.10881
585	0.03082	0.03340	0.03407	0.03699	0.03702	0.03981	0.04108	0.03617	13.2372	0.10059
595	0.03085	0.03313	0.03324	0.03549	0.03609	0.03836	0.03989	0.03529	9.9623	0.08943
605	0.03050	0.03226	0.03125	0.03464	0.03428	0.03627	0.03816	0.03391	7.6228	0.08142
615	0.02985	0.03160	0.03042	0.03328	0.03282	0.03471	0.03672	0.03277	5.8458	0.07378
625	0.02811	0.03044	0.02970	0.03236	0.03143	0.03365	0.03551	0.03160	6.2016	0.07881
635	0.02816	0.02890	0.02849	0.03202	0.02920	0.03266	0.03461	0.03058	6.2647	0.08185
645	0.02704	0.02835	0.02805	0.03096	0.02974	0.03174	0.03431	0.03003	6.3076	0.08364
655	0.02640	0.02692	0.02684	0.02906	0.02801	0.03006	0.03245	0.02845	4.7018	0.07599
665	0.02487	0.02602	0.02552	0.02716	0.02656	0.02746	0.03002	0.02680	2.8280	0.06275
675	0.02400	0.02475	0.02444	0.02625	0.02537	0.02618	0.02864	0.02566	2.4418	0.06089
685	0.02417	0.02074	0.02444	0.02642	0.02516	0.02620	0.02880	0.02564	2.7542	0.06473
695	0.02401	0.02387	0.02430	0.02575	0.02484	0.02638	0.02881	0.02542	3.0871	0.06911
712	0.02258	0.02074	0.02351	0.02366	0.02089	0.02408	0.02626	0.02310	3.6849	0.08309
737	0.01089	0.00860	0.01043	0.01190	0.00995	0.01190	0.01380	0.01107	2.7665	0.15029
762	0.00711	0.00773	0.00797	0.00868	0.00689	0.00867	0.00933	0.00805	0.7947	0.11067
787	0.00674	0.00715	0.00785	0.00829	0.00620	0.00769	0.00849	0.00749	0.6894	0.11088
812	0.00769	0.00755	0.00825	0.00899	0.00672	0.00864	0.01031	0.00831	1.3455	0.13962
837	0.00508	0.00495	0.00618	0.00718	0.00547	0.00693	0.00758	0.00620	1.1267	0.17133
862	0.00344	0.00492	0.00493	0.00539	0.00361	0.00547	0.00552	0.00475	0.7647	0.18397
887	0.00317	0.00368	0.00463	0.00497	0.00282	0.00474	0.00503	0.00415	0.8309	0.21980
912	0.00269	0.00339	0.00351	0.00433	0.00207	0.00444	0.00453	0.00357	0.8864	0.26384
937	0.00178	0.00357	0.00343	0.00340	0.00179	0.00411	0.00491	0.00328	1.3230	0.35029
962	0.00103	0.00240	0.00150	0.00194	0.00033	0.00362	0.00232	0.00188	1.1230	0.56469
987	0.00045	0.00109	0.00062	0.00245	-0.00019	0.00167	0.00169	0.00111	0.8010	0.80605
1012	0.00017	0.00095	0.00145	0.00245	-0.00027	0.00141	0.00166	0.00112	0.8498	0.82496
1037	0.00015	0.00095	0.00121	0.00238	-0.00031	0.00162	0.00154	0.00108	0.8341	0.84765
1062	0.00031	0.00212	0.00217	0.00280	-0.00014	0.00178	0.00195	0.00157	1.1417	0.68119
1087	0.00067	0.00212	0.00217	0.00280	0.00055	0.00193	0.00300	0.00190	0.9349	0.50796

Table B.6 - Volume Reflectance from the Dockside Water